

Fe Skarn, Iron Oxide Cu-Au, and Manto Cu-(Ag) Deposits in the Andes Cordillera of Southwest Mendoza Province (34°–36°S), Argentina

M.B. FRANCHINI^{1,2,†}, R.E. DE BARRIO³, M.J. PONS^{1,2}, I.B. SCHALAMUK^{1,3}, F.J. RIOS⁴, AND L. MEINERT⁵

(Received April 6, 2006; accepted June 14, 2007)

Abstract—Several Fe, Fe-Cu, and Cu-Ag prospects hosted by Mesozoic carbonate-rich sedimentary rocks that were intruded by diorite stocks define an approximately 20 × 200 km belt along the Andes Cordillera of southwest Mendoza province, Argentina (34°–36°S). This belt includes the Hierro Indio and Vegas Peladas Fe skarns, Las Choicas, and several other Cu-(Ag) prospects.

The main features of the Fe skarns include: association with mantle-derived middle Miocene (~15–11 Ma) diorite stocks and sills; widespread alteration including epidote ± amphibole ± magnetite endoskarns, and zoned garnet (Grs_{0-66} $\text{Adr}_{32.5-100}$) ± magnetite ± pyroxene (Di_{24-50} Jo_{2-9} Hd_{74-41}) exoskarns formed from oxidized, saline, high-temperature brines (530°–660°C; 60–70 wt.% NaCl equiv.); and magnetite-hematite orebodies associated with quartz ± epidote ± calcite ± actinolite formed at lower temperatures (290°–436°C) from saline fluids (32–50 wt.% NaCl equiv.) of magmatic origin.

West of the Fe skarn belt, the Valle Hermoso district covers more than 300 km² and hosts several poorly known Cu-(Ag) prospects (estimated 30 Mt with 1.5% Cu and 20 g/t Ag). These prospects share many characteristics with the iron oxide copper-gold-type systems and manto-type Cu deposits of northern and central Chile. One of the prospects (Las Choicas) is located at the apex of a regional 015°-trending anticline, along the contact of stratified carbonaceous sandstone and limestone (Neocallovian-Oxfordian) with a diorite pluton. This pluton has positive Ta and Nb anomalies (on normalized diagrams) and a high Ti content, features uncommon in Miocene diorites associated with Fe skarns and of magmas derived from sub-arc mantle sources. Alteration at Las Choicas includes early widespread chlorite + calcite ± albite ± scapolite ± ilmenite or titanite ± apatite, and local actinolite ± hematite ± biotite alteration of diorite and sedimentary rocks along contacts. Later Cu mineralization (1%–10% Cu) is associated with calcite ± albite ± quartz alteration in fractures, vein networks, and crackle breccias. Mineralization is zoned from bornite ± chalcopyrite ± millerite with Zn, As, Mo, Ag, and U anomalies in the main orebody, through chalcopyrite-rich breccias with Zn anomalies, and chalcopyrite ± tetrahedrite vein networks with Sb, As, Ag, and Zn anomalies in the uppermost zone, to a Cu-depleted pyrite-rich envelope with Co anomalies, and finally to late, barren calcite veins in distal zones. © 2007 Canadian Institute of Mining, Metallurgy and Petroleum. All rights reserved.

Key Words: Fe skarns, manto Cu deposits, IOCG deposits, late Miocene, calc-alkaline diorite plutons, Cordillera Principal, southwest Mendoza.

Sommaire—Une série de plusieurs indices de Fe, Fe-Cu, et Cu-Ag dans des roches sédimentaires carbonatées Mésozoïques recoupées par des stocks de diorite forment une ceinture d'environ 20 × 200 km le long de la Cordillère des Andes dans la partie sud-ouest de la province de Mendoza, en Argentine (34°–36°S). Cette ceinture comprend les gîtes de fer de type skarn Hierro Indio et Vegas Peladas, Las Choicas et plusieurs autres indices de Cu-(Ag).

Les principales caractéristiques de ces skarns ferrifères sont : l'association avec des sills et des stocks de diorite dérivés du manteau au Miocène moyen (~15–11 Ma); une altération importante comprenant des endoskarns à épidoite ± amphibole ± magnétite, et des exoskarns à grenats zonés (Grs_{0-66} $\text{Adr}_{32.5-100}$) ± magnétite ± pyroxène (Di_{24-50} Jo_{2-9} Hd_{74-41}) formés par des saumures oxydées à haute salinité et à haute température (530°–660°C; 60–70 % poids NaCl équiv.); et des corps minéralisés constitués de magnétite et d'hématite associés à du quartz ± épidoite ± calcite ± actinolite formés à basse température (290°–436°C) par des fluides salins d'origine magmatique (32–50 % poids NaCl équiv.).

À l'ouest de cette ceinture de skarns ferrifères, on trouve le district de Valle Hermoso, lequel couvre plus de 300 km² et contient plusieurs indices mal connus de Cu-(Ag) (estimés à 30 Mt à une teneur moyenne de 1.5% Cu et de 20 g/t Ag). Ces indices partagent plusieurs caractéristiques des systèmes de type oxyde de fer-cuivre-or ou des gîtes de Cu de type manto du nord et du centre du Chili. Un de ces indices (Las Choicas) est situé à l'extrémité d'un anticlinal régional de direction N015°, le long d'un contact entre des grès calcaires intervertis avec des calcaires (Neocallovien-Oxfordien) et un pluton de diorite. Ce pluton présente des anomalies positives en Ta et en Nb (sur un diagramme normalisé) et un contenu élevé en Ti, ces caractéristiques sont inhabituelles chez les diorites du Miocène associées aux skarns ferrifères et aux magmas dérivés d'une source mantellique sous-jacente à un arc. L'altération à Las Choicas comprend une zone de chlorite + calcite ± albite ± scapolite ± ilménite ou titanite ± apatite précoces largement distribuée, et une altération locale de la diorite et des roches sédimentaires en actinolite ± hématite ± biotite le long des contacts. La minéralisation en Cu (1%–10% Cu) est plus tardive et associée avec une altération en calcite ± albite ± quartz dans des fractures, des réseaux de veines, et des brèches de dislocation. La minéralisation présente une zonalité comprenant le corps minéralisé principal constitué de bornite ± chalcopyrite ± millerite accompagné de teneurs anomalies en Zn, As, Mo, Ag, et U, une brèche riche en chalcopyrite accompagnée d'anomalies en Zn, un réseau de veines de chalcopyrite ± tétrahédrite avec des anomalies en Sb, As, Ag, et Zn dans la zone supérieure, une enveloppe pyriteuse appauvrie en Cu et anomale en Co et finalement une zone distale marquée par des veines de calcite stériles. © 2007 Canadian Institute of Mining, Metallurgy and Petroleum. All rights reserved.

¹ Consejo Nacional de Investigaciones Científicas y Técnicas (CONICET).

² Centro Patagónico de Estudios Metalogenéticos, CIMAR, Facultad de Ingeniería, Universidad Nacional del Comahue, Av. Buenos Aires 1400 (8300) Neuquén, Argentina.

³ Instituto de Recursos Minerales, Facultad de Ciencias Naturales y Museo, Universidad Nacional de La Plata, Calle 64 N° 3, 1900, La Plata, Argentina.

⁴ Centro da Desenvolvimento de Tecnologia Nuclear (CDTN-CNEN), Belo Horizonte, MG, Brazil.

⁵ Department of Geology, Smith College, Northampton, MA 01063, United States.

† Corresponding Author: mfranchi@uncoma.edu.ar

Introduction

One of the best developed iron oxide copper-gold (IOCG) provinces in the world is located in the South American Coastal Cordillera of Southern Perú and northern Chile (13° – $33^{\circ}30'$ S), closely associated with Mesozoic batholiths and major arc-parallel fault systems (Sillitoe, 2003, and references therein). The massive magnetite deposits of southern Perú (15° – $15^{\circ}30'$ S; Sillitoe, 2003) and northern Chile (25° – 31° S; Nyström and Henríquez, 1994), and the manto-type Cu-(Ag) deposits of the Coastal Cordillera of northern and central Chile (Espinoza et al., 1996) occupy the same belt as many of the IOCG deposits. Because these two deposit types have several similarities with IOCG deposits, some authors include them as end-member categories of the IOCG clan (Hitzman et al., 1992; Vivallo and Henríquez, 1998; Williams, 1999; Pollard, 2000).

Numerous Fe, Fe-Cu, and Cu-(Ag) prospects similar to the above-mentioned Peruvian and Chilean deposits also occur in Argentina, in an approximately 20 km-wide and 200 km-long belt along the south-central Andes segment known as the Cordillera Principal of southwest Mendoza province (Ramos, 1993; Fig. 1, Table 1). Some of these prospects were mined for Fe, Cu, and Ag on a small scale in the early 1900s (Las Choicas: Centeno and Fallet, 1999; Hierro Indio: Zanettini, 1999), but little is known about their genesis. Most of these prospects have been described as Fe and Cu skarns (see Table 1), although the Las Choicas and other Cu-(Ag) prospects of the Valle Hermoso district are different in their alteration style and mineralization.

This contribution documents the most important Fe and Cu deposits in southwest Mendoza province, based on a synthesis of the available literature summarized in Table 1 (modified from Franchini and Dawson, 1999; Franchini, 2005) and investigation of surface exposures. We focus on two Fe skarn districts, Hierro Indio and Vegas Peladas, and the Las Choicas Cu-(Ag) prospect in order to understand existing deposits and to develop new exploration models for this poorly known part of the Argentinean Cordillera. The Las Choicas Cu-(Ag) and other Cu-(Ag) prospects of the Valle Hermoso district share several features characteristic of the IOCG deposits

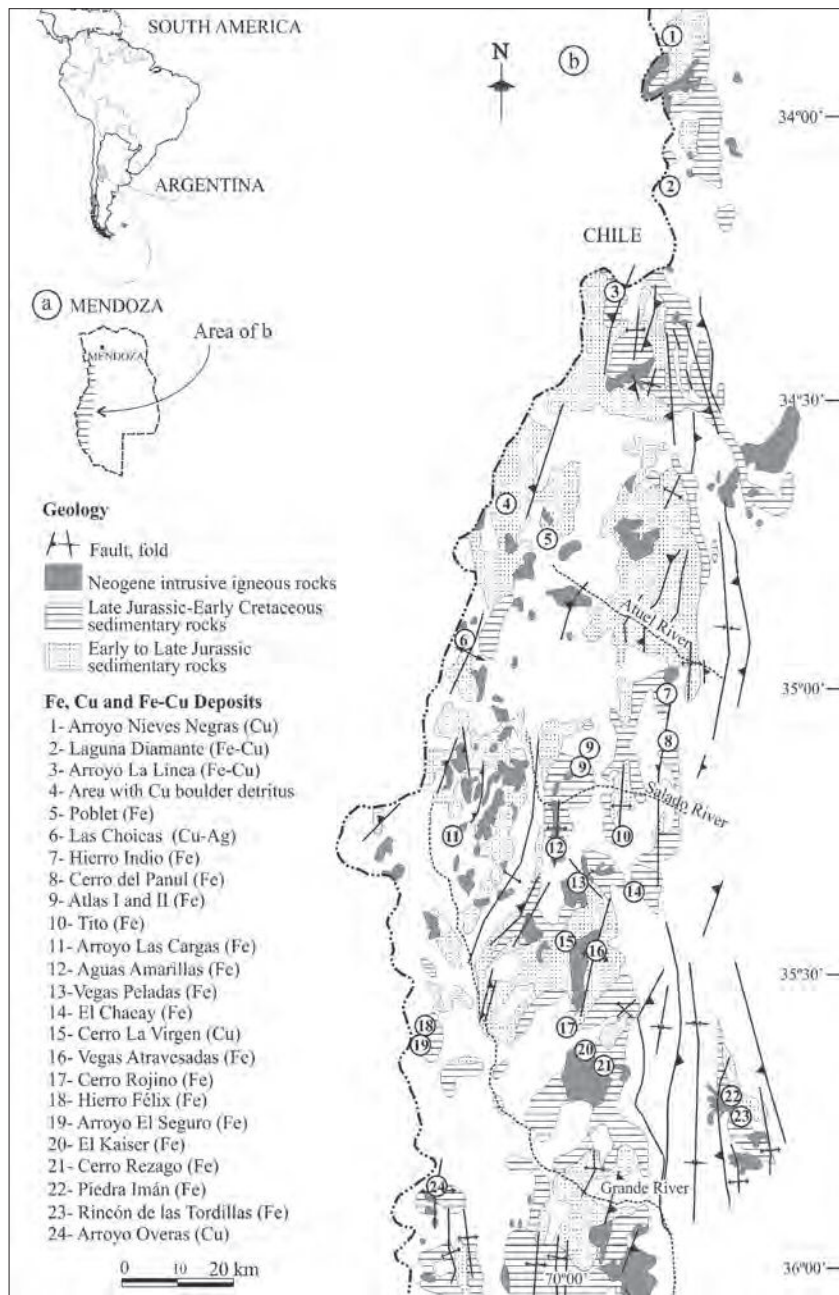


Fig. 1. Location of Fe skarns, Las Choicas, and other Cu prospects in Mendoza province of central western Argentina. **a.** The streaky outlined pattern represents the fold and thrust belt of Malargüe (34° – 36° S), Cordillera Principal of SW Mendoza. **b.** Geological map of the thrust belt of Malargüe, modified from Kozlowski et al. (1993), Ramos and Nullo (1993), and Mendez et al. (1995), showing Mesozoic lithologies, Neogene igneous rocks associated with Fe, Fe-Cu, and Cu deposits, and the main structures of the area.

of Perú and Chile (as summarized by Sillitoe, 2003, and Williams et al., 2005), and also of the manto-type Cu deposits of northern and central Chile (Espinoza et al., 1996). If this is the case, this is the first description of IOCG and manto-type deposits in this segment of the Andes Cordillera of Argentina, and implies that geologic conditions that favor the development of these deposits may be more widespread than previously thought. The presence of other poorly known Cu-Fe districts located near the Chilean bor-

der (Fig. 1) suggests significant future exploration potential for IOCG and manto-type Cu mineralization in this area.

Samples and Analytical Methods

This study is based on 395 samples collected from mapped outcrops. Samples were analyzed by transmitted and reflected light petrography and X-ray diffraction (Rigaku-DII-Max) at the Center for Investigation of Clay Minerals, University Nacional del Comahue (Neuquén, Argentina). Mineral compositions were determined by electron microprobe analyses ($n = 220$) at the Centro de Desenvolvimento da Tecnologia Nuclear (CDTN, CNEN, Belo Horizonte, Brazil, using a Jeol-JXA-8900 RL WD/ED microprobe), at the Scientific-Technical Services of the Barcelona University (Cameca SX50), and at the laboratory in the Geology Department, Oviedo University, Spain (Cameca, SX50).

Microthermometric analyses of fluid inclusions (250 inclusions) in quartz, garnet, and pyroxene were carried out using Chaixmeca -180°/600°C fluid inclusion cooling-heating stages at the Fluid Inclusion Laboratory in the Department of Geology, Del Sur National University (Bahía Blanca, Argentina). Homogenization temperatures higher than 550°C were measured with a Leitz Wetzlar heating stage 1350 for melt inclusions, with control system Heinzeinger 16-30, at the Centro de Desenvolvimento da Tecnologia Nuclear (CDTN, Belo Horizonte, Brazil). Homogenization temperatures and salinities of fluid inclusions in calcite from the Hierro Indio skarn were obtained using a Chaixmeca Eurotherm at the Laboratorio da Inclusiones Fluidas of the Centro de Desenvolvimento da Tecnologia Nuclear (CDTN, Belo Horizonte). Synthetic standards from Bubbles Inc. were used to calibrate microthermometric analyses using the Leitz Wetzlar and Chaixmeca stages.

Thirty-five samples of least-altered protoliths (igneous and sedimentary rocks) were analyzed for major and trace elements by inductively coupled plasma-emission spectrometry (ICP-ES), ICP-mass spectrometry (ICP-MS), and X-ray fluorescence, respectively, at Acme Analytical Laboratories Ltd. (Canada), at Alex Stewart Assayers Ltd. (Ireland), and at the Instituto de Geociencias of the São Paulo University (Brazil).

Seven samples of the Vegas Peladas mineralized skarn were analyzed for base and precious metals by ICP-ES, and for Au by fire assay (atomic absorption spectrometry), at Acme Analytical Laboratories (Canada). Twenty-one samples of altered and mineralized protoliths from Las Choicas Cu prospect were analyzed for 41 trace elements by ICP-ES (on a previous dissolution with aqua regia) and for Au by fire assay (atomic absorption spectrometry) at Alex Stewart Assayers Ltd. (Argentina). Thirteen samples with higher Cu grades were analyzed by ICP-ES on previously dissolved samples with an oxidizing digestion and final dissolution in aqua regia (precision $\pm 5\%$).

Radiometric ages for three igneous rocks samples (Hierro Indio and Vegas Peladas diorites, and Vegas Peladas granodiorite) were determined by $^{40}\text{Ar}/^{39}\text{Ar}$ in plagioclase, and $^{87}\text{Rb}/^{86}\text{Sr}$ in whole rock and biotite, at the CPGeo-Cen-

tro de Pesquisas Geocronológicas, Instituto de Geociencias, São Paulo University, Brazil. Radiometric ages for two samples of the Las Choicas diorite were also determined by $^{40}\text{Ar}/^{39}\text{Ar}$ in plagioclase, and K/Ar in whole rock at the Laboratorio de Geocronología of the SERNAGEOMIN (Servicio Nacional de Geología y Minería, Chile).

Regional Geologic Setting: Lithological and Structural Controls

The study area is located in the Andes Cordillera, an active continental margin of southwestern South America (Fig. 1). This mountain belt is the result of a complex history of Mesozoic and Cenozoic sedimentation, magmatism, and tectonic deformation superimposed on a Paleozoic basement characterized by multiple accretion events that started in the Neoproterozoic (Mpodozis and Ramos, 1998; Ramos, 1999 a,b). The deposits are located in the fold and thrust belt of Malargüe (34°–36°S; Kozlowski et al., 1993; Mingramm et al., 1993), in the central-south Andes segment known as Cordillera Principal of southwest Mendoza province (Ramos, 1993). The Benioff zone beneath this segment of the Andes appears to have dipped at about 30° throughout the late Cenozoic (Ramos and Nullo, 1993).

During the Late Triassic–early Tertiary, the structural setting of the region was characterized by a series of fault-bounded depressions located east of the arc-trench system, and the tectonic regime was dominated by back-arc extension and subsidence with local episodes of uplift, folding, and erosion (Gulisano and Gutiérrez Pleimling, 1995). More than 6000 m of Late Triassic to Paleocene marine and continental sedimentary rocks unconformably overlie the Permian–Triassic volcanioclastic basement of the Choiyoi Group. Compressional tectonics, typical of Chilean-type subduction, began in the Tertiary (Gulisano and Gutiérrez Pleimling, 1995), forming the Malargüe thrust belt (Kozlowski et al., 1993). This compression was followed by widespread volcano-plutonic activity, represented in this segment by three magmatic cycles (Ramos and Nullo, 1993): the late Eocene to early Oligocene Molle Group (Haller et al., 1985; Nullo, 1985); the widespread Miocene Huincán Formation (Nullo, 1985; Bouza, 1991; Baldauf et al., 1992); and young Pleistocene volcanism (Ramos and Nullo, 1993). Typical Cordilleran I-type plutons were emplaced into the Mesozoic–Cenozoic sedimentary sequences along the main (N–S) thrust faults and folds (Ramos and Nullo, 1993).

Sedimentary Host Rocks

The stratigraphic column of the Malargüe fold belt (modified from Legarreta et al., 1993) and the occurrence of Fe, Fe-Cu, and Cu skarns and Las Choicas Cu-(Ag) prospect in each lithology are summarized in Figure 2 and Table 1 (modified from Franchini and Dawson, 1999; Franchini, 2005). The majority of the Fe skarns occur in limestone, although other host rocks include siltstone, mudstone, calcareous siltstone, and minor sandstone.

Two Fe skarn prospects are hosted in the Calabozo Formation (early–middle Callovian; Legarreta et al., 1993),

Table 1. Fe, Fe-Cu, and Cu Prospects Located in the Cordillera Principal of SW Mendoza Province

#	Deposit Name	Latitude	Longitude	Size & Grade	Igneous Rocks
1	Ao. Nieves Negras (Cu)	33°51'S	69°51'W		Neogene calc-alkaline magmatism; Andesite dikes and diorite stock
2	Laguna Diamante (Fe-Cu)	34°06'S	69°51'W	Geochemical sampling in moraine: 100–1000 ppm Cu; 20–100 ppm Zn; Up to 56 ppm Mo	Neogene calc-alkaline magmatism; Porphyritic granodiorite
3	Arroyo La Línea (Fe-Cu)	34°18'S	69°57'W		Neogene calc-alkaline porphyritic granodiorite-monzonite
4	Cu boulder detritus (Cu)	34°41'S	70°14'30"W	2.68 wt.% Cu in boulders in an area with thick modern cover	
5	Poblet (Fe)	34°44'56"S	70°06'W	0.125 Mt with 54–57 wt.% Fe in magnetite-rich zones; Small underground working	Neogene calc-alkaline magmatism; Porphyritic andesite to trachyte
6	Las Choicas (Cu-Ag)	34°54'55"S	70°16'40"W	0.4 Mt with 4.27 wt.% Cu and 30 g/t Ag; 1.7–10 wt.% Cu; 0.3–0.4 wt.% Ni; 153–275 ppm Cr; Up to 0.2 wt.% Zn; 79 ppm Mo; 48–344 ppm Ag; 133 ppm U; Up to 1.5 wt.% As, 0.96 wt.% Sb, 0.1 wt.% Ba; 2 km underground working, 23 drill holes	Calc-alkaline magmatism, diorite stock; Chlorite, calcite, albite, apatite, local actinolite, hematite, biotite; Calcite, albite, quartz
7	Hierro Indio (Fe)	34°59'S	69°47'W	0.45 Mt with 63 wt.% Fe; Open-pit mine	11 ± 1 Ma calc-alkaline diorite stock and porphyritic andesite sills; Actinolite, calcite, albite, titanite pyroxene ($\text{Di}_{79-88}\text{Jo}_{0.3-0.5}$), apatite
8	Cerro del Panul (Fe)	35°04'30"S	69°47'W	Thick modern cover	Neogene calc-alkaline magmatism
9	Atlas I and II (Fe)	35°05'30"S	69°58'W	0.016 Mt with 36 wt.% Fe and 11 wt.% Mn in outcrops	Neogene calc-alkaline porphyritic andesite
10	Tito (Fe)	35°14'S	69°52'W	Preliminary sampling, 62 wt.% Fe	Neogene calc-alkaline granodiorite stock
11	Ao. Las Cargas (Fe)	35°14'30"S	70°18'30"W	14–54 wt.% Fe; 0.025–0.26 wt.% Cu, 50–200 ppm Bi, 60–5000 ppm Zn, <500 ppm As, <50 ppm Au	Neogene calc-alkaline andesite sills and diorite stock
12	Aguas Amarillas (Fe)	35°15'S	70°01'30"W	0.3–14 wt.% Fe, 8–460 ppm Ni, 2–400 ppm Cu, 14–116 ppm Co, 180–460 ppm Zn, 20–90 ppm Pb, 0.3–3.5 ppm Ag	14.7 ± 1.7 to 13 ± 1.0 Ma calc-alkaline diorite to granodiorite stock and sills; Scapolite, pyroxene, vesubianite, garnet
13	Vegas Peladas (Fe)	35°20'30"S	69°56'25"W	39–69.5 wt.% Fe	15.19 ± 0.24 Ma calc-alkaline diorite stock; Amphibole, chlorite, calcite; Orthoclase, quartz, epidote, amphibole; Epidote, calcite
14	El Chacay (Fe)	35°20'30"S	69°50'30"W	56.6 wt.% Fe; In diorite: 20–80 ppm Cu, 14–116 ppm Co, 14–40 ppm Pb, 20–60 ppm Zn, 4–8 ppm Mo	Neogene calc-alkaline diorite stock with argillic alteration; Widespread alteration zone upwards along the Chacay creek
15	Cerro de la Virgen (Cu)	35°24'30"S	70°01'W	Bench I: 5.66 wt.% Cu and 105 g/t Ag; Bench II: 2.5 wt.% Cu and 30 g/t Ag	Neogene calc-alkaline diorite stock crosscut by andesite dikes
16	Vegas Atravesadas (Fe)	35°26'30"S	69°56'W	Pb anomalies	Neogene calc-alkaline, fine-grained diorite stock, and andesite dikes
17	Cerro Rojino (Fe)	35°34'30"S	70°00'30"W	58.6 wt.% Fe	Neogene calc-alkaline andesite to traqu-andesite dikes
18	Hierro Felix (Fe)	35°34'30"S	70°20'30"W	55.8 wt.% Fe, <5000 ppm Zn, 120 ppm Cu, <250 ppm Pb, <5000 ppm As, <250 ppm Sb, <50 ppm Au, 250 ppm Bi in few samples	Neogene calc-alkaline andesite dikes; Calcite, chlorite, pyrite
19	Arroyo El Seguro (Fe)	35°37'S	70°23'W	Cu, Pb, and Zn anomalies in drainage sampling; Up to 0.2 wt.% Pb in breccia with Zn anomalies	Neogene calc-alkaline andesite dikes; Quartz, pyrite
20	El Kaiser (Fe)	35°38'30"S	69°55'W	0.100 Mt. with 58 wt.% Fe, 130–2300 ppm Cu, 110–440 ppm Pb, 120–660 ppm Zn	11.7 ± 1.3 Ma calc-alkaline, metaluminous andesite dikes and sills
21	Cerro Rezago (Fe)	35°39'S	69°55'W	40–62 wt.% Fe	Neogene calc-alkaline andesite dikes and sills; Kaolinite, pyrite
22	Piedra Imán (Fe)	35°42'S	69°35'30"W	40–51 wt.% Fe	Neogene calc-alkaline andesite dikes and sills with amphibole
23	Rincón de las Tordillas (Fe)	35°42'30"S	69°35'W	41–68 wt.% Fe in few samples	Neogene calc-alkaline andesite dikes and sills; Kaolinite
24	Arroyo Overas (Cu)	35°52'S	70°19'30"W	80 and 1000 ppm Cu, 220 ppm Zn, and 40 ppm Pb in some samples	Neogene calc-alkaline diorite stock

Notes

Adr = andradite, Alm = almandine, Di = diopside, Jo = johannsenite, Sps = spessartine.
See deposit locations in Fig. 1b.

Table 1. (Continued)

Sedimentary Rocks	Ore Mineralogy	References
Lower Cretaceous limestone; Quartz	Pyrite, chalcopyrite, pyrrhotite	Naciones Unidas (1970)
Upper Jurassic–Lower Cretaceous sandstone, shale and limestone; Pyroxene, garnet, epidote, scapolite; Quartz, tourmaline veins and breccia	Magnetite, pyrite, pyrrhotite, chalcopyrite; Malachite, azurite	Naciones Unidas (1970)
Middle–Upper Jurassic limestone, gypsum, shale; Epidote > garnet, pyroxene, scapolite, calcite Cu sulfosalts	Pyrite, chalcopyrite, magnetite, hematite	Naciones Unidas (1970) Zanettini (1984)
Middle–Upper Jurassic limestone; Garnet > epidote; Amphibole, calcite, quartz	Magnetite > hematite, pyrite > chalcopyrite	La Rocque (1964); Angelelli (1984)
Upper Jurassic limestone; Chlorite, calcite, albite, scapolite, titanite, apatite; Calcite, albite, quartz; barite, calcite, siderite	Bornite, chalcopyrite, ilmenite, pyrite, hematite, tetrahedrite, sphalerite; Chalcocite, covellite; Malachite, azurite, cuprite	Devito (1954); Zanettini (1984); Angelelli (1984); Centeno and Fallet (1999); Cominor Ing. y proyectos S.A. (1999); This study
	Hematite > magnetite >> pyrite; Malachite, azurite, chrysocolla	Rigal (1942); Elizalde and Laguinge (1954); Bonfils (1972); Angelelli (1984); Zanettini (1999); Dawson et al. (2000); This study
Lower Cretaceous fossiliferous limestone and sandstone; Skarn not described	Magnetite and boulders	La Rocque (1964); DGFM (1969)
Lower Cretaceous fossiliferous limestone and sandstone	Hematite, Mn oxides	La Rocque (1964); DGFM (1969)
Lower Cretaceous limestone and sandstone; Breccia	Hematite, pyrrhotite	Fallet (1972)
Lower Cretaceous fossiliferous limestone and calcareous shale; Epidote, calcite	Magnetite, hematite > pyrite, chalcopyrite; Malachite	DGFM (1969); Zanettini (1984)
Lower Cretaceous fossiliferous calcareous shale; Pyroxene, wollastonite, scapolite > garnet; Amphibole, albite, epidote; Quartz, calcite, fluorite	Pyrrhotite > pyrite, chalcopyrite, hematite, marcasite	DGFM (1969); Lurgo and Zappetini (1987); Nullo et al. (2002)
Lower–Middle Jurassic limestone, shales and mudstone; Garnet ($Adr_{52-100} Sp_{-}Alm_{0-2}$) >> pyroxene ($Di_{24-50} Jo_{2-9}$), quartz; Epidote, actinolite	Magnetite, hematite, mushketovite >> pyrite	Peña (1955); DGFM (1969); Arrospide (1972); Zanettini (1984); This study
Lower Cretaceous limestone; Garnet, epidote, wollastonite; Calcite, feldspar, chlorite	Hematite, pyrite	Barriónuevo and Elizalde (1950); La Roque (1964)
Lower Cretaceous silty and sandy limestone; Garnet, pyroxene; Chalcopyrite, pyrite; Malachite, azurite Epidote, calcite		Angelelli (1950); Barriónuevo (1953)
Lower–Middle Jurassic limestone and marl; Epidote, calcite	Magnetite, hematite	Angelelli (1950); Barriónuevo and Elizalde (1950); Peña (1955); DGFM (1969)
Lower Cretaceous limestone	Magnetite	Barriónuevo and Elizalde (1950); La Rocque (1964)
Lower Cretaceous limestone; Epidote, calcite	Magnetite, pyrite	DGFM (1969); La Rocque (1964); Tabachi and Elizalde (1961)
Lower Cretaceous limestone metasediments; Calcareous breccia	Hematite, magnetite, pyrite, chalcopyrite, pyrrhotite	Naciones Unidas (1970); Wippern (1974)
Lower Cretaceous limestone; Epidote >> garnet, calcite; Breccia with calcite and magnetite cement	Magnetite >> pyrite	Peña (1955); DGFM (1969); Angelelli et al. (1970); Naciones Unidas (1970); Dessanti (1973); Pons et al. (2004)
Lower Cretaceous limestone; Epidote, calcite	Hematite, magnetite, pyrite	Barriónuevo and Elizalde (1950); La Roque (1964); DGFM (1969)
Lower Cretaceous limestone; Epidote >> garnet, calcite	Magnetite, hematite, pyrite	Barriónuevo and Elizalde (1950); Peña (1955); DGFM (1969); Dessanti (1973)
Lower Cretaceous fossiliferous limestone; Epidote, quartz	Hematite	Barriónuevo and Elizalde (1950); Peña (1955)
Lower Cretaceous limestone	Pyrrhotite, pyrite, Ni sulfides, chalcopyrite, hematite	La Rocque (1964); Naciones Unidas (1970)

STRATIGRAPHIC COLUMN OF SW MENDOZA

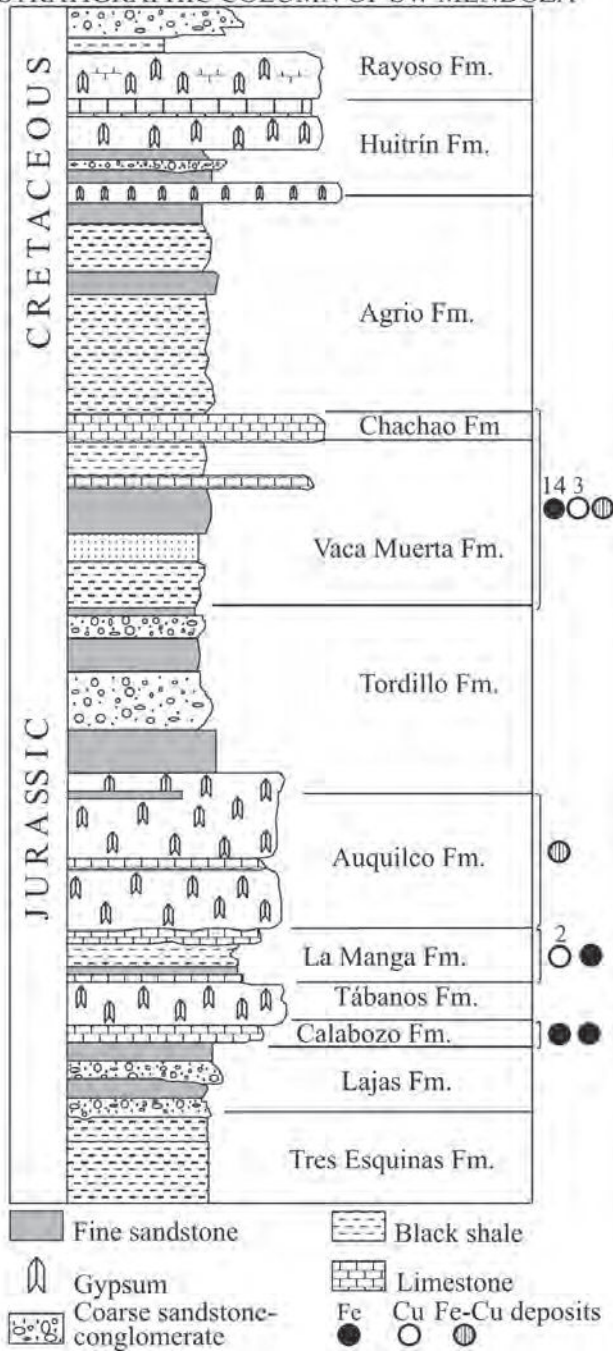


Fig. 2. Detail of the Mesozoic stratigraphic column (modified from Legarreta et al., 1993) in the thrust belt of Malargüe, with the distribution of the Fe, Fe-Cu, and Cu deposits (after Franchini and Dawson, 1999; Franchini, 2005).

which comprises skeletal and oolitic limestone with abundant invertebrate fauna, and which grades laterally into medium- and coarse-grained clastic sediments deposited in a shallow carbonate shelf environment. One Fe skarn, the area with Cu boulder detritus, and the Las Choicas Cu prospect are hosted in the La Manga Formation (Neocallonian–Oxfordian), which comprises micritic and sparitic

limestone and claystone deposited in a shelf environment, and which grades upward to well-stratified calcareous sandstone, limestone, conglomerates, and clastic sediments with abundant volcanic-derived components (Legarreta et al., 1993). One Fe-Cu skarn occurs in the Auquilco Formation (late Oxfordian), an evaporitic succession with intercalations of micritic limestone and minor detrital material deposited in a shallow marine hypersaline environment. The other fourteen Mendoza Fe skarns, one Fe-Cu skarn, and three Cu skarns are hosted by the lower members of Mendoza Group, consisting of Tithonian–lower Valanginian basinal and offshore black shales, claystone, marl, and micritic limestone of the Vaca Muerta Formation, and in sublitoral marine skeletal limestone of the Chachao Formation (Valanginian–Berriasian; Legarreta et al., 1993).

Associated Igneous Rocks

Fe skarns of southwestern Mendoza province are associated with Tertiary stocks and numerous related micro-porphyritic to porphyritic sills and dikes, which are rich in plagioclase, amphibole, and magnetite. Based on previously published data (Ramos and Nullo, 1993; Nullo et al., 2002, and references therein) and recent radiometric dating, their ages range from 15 ± 3 Ma to 11.8 ± 0.7 Ma ($^{40}\text{Ar}/^{39}\text{Ar}$ in plagioclase), and therefore belong to the Miocene Huincán eruptive cycle of the Neogene arc (Ramos and Nullo, 1993). Geochemically, these igneous rocks are similar to plutons associated with iron skarns (cf. Meinert, 1995): they are intermediate composition (diorite), metaluminous, and subalkaline with a calc-alkaline affinity (Fig. 3a-d). They contain more MgO (0.90–4.16 wt.%), less K₂O (0.4–1.9 wt.%), and less SiO₂ (52.7–61.8 wt.%; Table 2) than igneous rocks typically associated with Cu and Zn skarns (Meinert, 1995). Trace element contents such as Sc (7–23 ppm), V (40–209 ppm) and low Rb/Sr ratios (0.01–0.11), are similar to Fe skarn-related plutons (Table 2).

The N-MORB normalized trace element patterns (Pearce, 1996) of all the rocks show negative Ta and Nb anomalies with respect to Th and Ce, low Hf and Zr, and depletion in Ti, characteristics of calc-alkaline magmas derived from a sub-arc mantle source (Fig. 3e; Kay and Mpodozis, 2002). Trace element and rare earth element (REE) contents of the Neogene igneous rocks are similar to the Andean Quaternary volcanic rocks of the Transitional Southern Volcanic Zone (TSVZ, 34°S to 37°S), Planchón-Peteroa (35°S), and Nevados de Chillán Volcanic Group (36°55'S) that were emplaced in a relatively thin continental crust (35 km; Davison et al., 1988; Hildreth and Moorbath, 1988; Tormey et al., 1991; Franchini et al., 2003; Fig. 3g,h).

As in the case of the TSVZ basalts, subcrustal sources and processes can be modeled by approximately 10% melting of a peridotitic mantle source enriched in alkalis (among them Cs coming from subducted pelagic sediments; Morris and Hart, 1983; Futa and Stern, 1988) and alkali earth elements by fluids coming from the subducted oceanic slab (López-Escobar et al., 1995). The initial $^{87}\text{Sr}/^{86}\text{Sr}$ ratio of 0.704351 ± 0.000044 and preliminary $^{147}\text{Sm}/^{144}\text{Nd}$ and

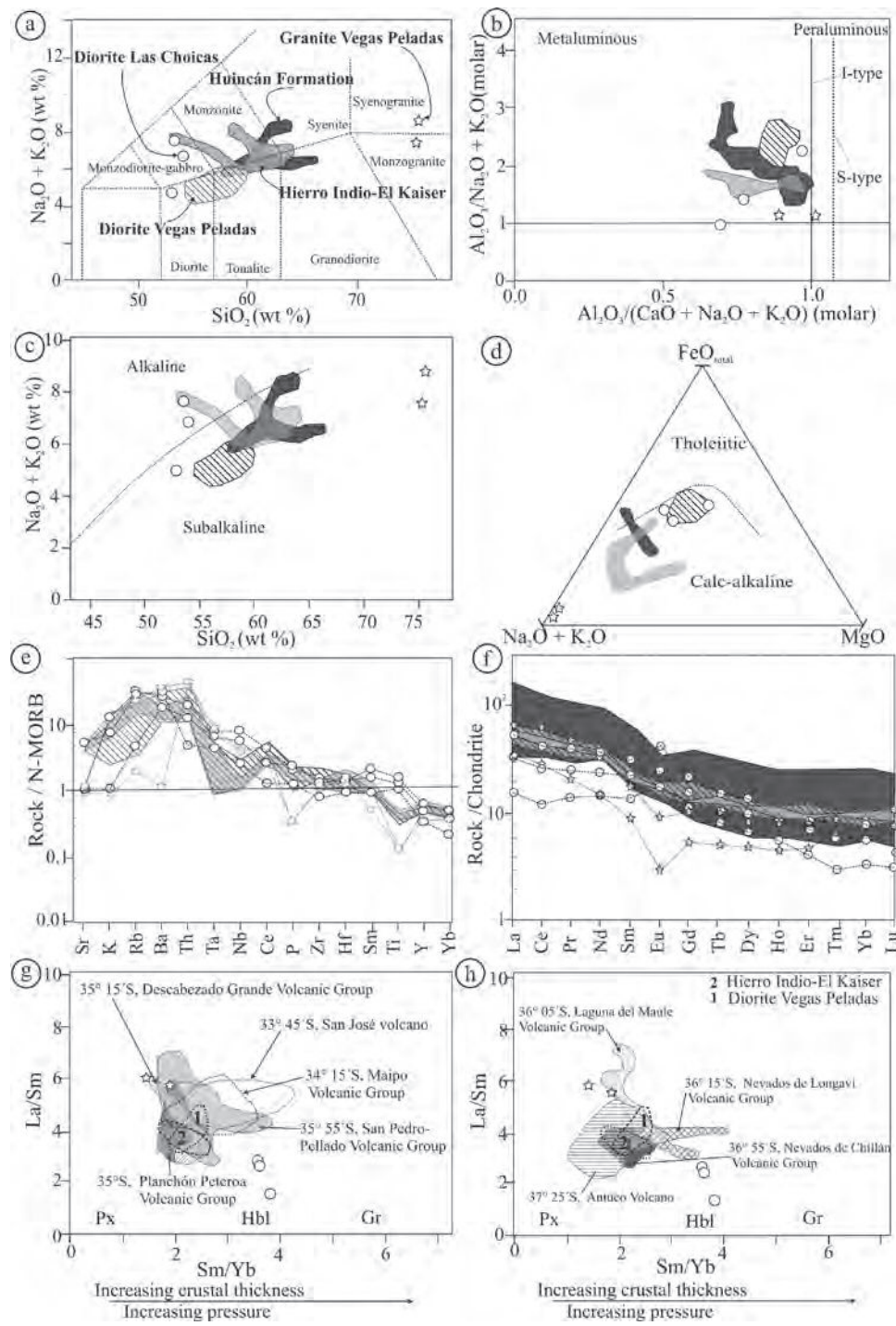


Fig. 3. Chemical characterization of least-altered Hierro Indio and Vegas Peladas igneous rocks associated with Fe skarns and the Las Choicas Cu prospect. The composition of other igneous rocks from the Neogene Huincán Formation (dark gray; after Nullo et al., 2002), from El Kaiser Fe skarn (light gray; Pons et al., 2004), and the Vegas Peladas diorite (cross-hatched) are shown for comparison. **a.** Total alkali-silica classification (Middlemost, 1994; Bellieni et al., 1996). **b.** Aluminum saturation index. **c.** $\text{Na}_2\text{O} + \text{K}_2\text{O}$ versus SiO_2 . **d.** AFM diagram with calc-alkalic-tholeiitic boundary line from Irvine and Baragar (1971). **e.** Whole-rock trace element concentrations normalized to N-type MORB (Pearce, 1996) showing differences in the Nb and Ti anomalies. **f.** Whole-rock REE diagram normalized to average chondrite (Boynton, 1989). **g,h.** La/Sm vs. Sm/Yb ratios for Vegas Peladas, Hierro Indio and Las Choicas igneous rocks compared with those from SVZ (data of San Pedro-Pellado volcanic complex from Davidson et al., 1988; other SVZ data from Leopoldo López Escobar, in Franchini et al., 2003). This diagram illustrates the relationship between REE patterns and crustal thickness (Hildreth and Moorbath, 1988).

Table 2. Whole-rock Major and Trace Element Compositions of Representative Diorite, Granite, and Rhyolite Samples from Hierro Indio, Vegas Peladas, and Las Choicas

Sample	Hierro Indio										Vegas Peladas										Las Choicas														
	Diorite					Diorite					Rhyolite					Granite					Fe skarns					Diorite									
	*	2601	*	*	*	*	*	*	*	*	*	*	*	*	*	*	*	*	*	*	*	*	*	*	*	*	*	*	*	*	***	***			
(wt. %)																																			
SiO ₂	57.39	61.78	61.37	52.70	56.29	55.91	53.73	54.84	54.81	56.49	54.78	56.74	55.15	56.81	58.85	74.03	74.60	59.30	47.00	75.60	53.40	53.01	54.20												
Al ₂ O ₃	17.09	17.95	17.86	17.30	18.17	17.52	18.60	18.38	18.30	17.77	18.51	17.93	17.53	17.24	17.40	13.85	14.25	16.80	12.20	22.70	16.11	16.46	14.94												
TiO ₂	0.83	0.60	0.65	0.79	0.87	0.83	0.79	0.86	0.79	0.75	0.98	0.73	0.71	0.69	0.58	0.42	0.42	0.19	0.80	0.10	3.10	1.81	1.54	2.28											
Fe ₂ O ₃ ^T	3.09	1.67	3.76	2.48	7.70	7.36	9.04	8.16	8.27	8.17	8.53	7.78	8.15	7.28	6.94	0.58	—	—	—	—	—	—	—	—	—	—	—	—	—	—	—	—			
Fe ₂ O ₃	—	—	—	—	—	—	—	—	—	—	—	—	—	—	—	—	—	—	—	—	—	—	—	—	—	—	—	—	—	—	—				
FeO	—	—	—	—	—	—	—	—	—	—	—	—	—	—	—	—	—	—	—	—	—	—	—	—	—	—	—	—	—	—	—				
MnO	0.08	0.06	0.11	0.08	0.15	0.09	0.12	0.16	0.16	0.16	0.08	0.13	0.13	0.12	0.10	0.02	0.02	0.02	0.02	0.02	0.02	0.02	0.02	0.02	0.02	0.02	0.02	0.02	0.02	0.02	0.02	0.02			
MgO	3.81	1.66	0.87	2.01	2.80	3.08	3.05	2.98	3.01	2.70	2.97	2.69	4.16	3.77	2.86	0.19	0.10	0.20	0.20	0.20	0.20	0.20	0.20	0.20	0.20	0.20	0.20	0.20	0.20	0.20	0.20	0.20			
CaO	9.44	8.03	5.10	6.65	7.03	6.12	7.26	7.62	7.27	7.06	7.14	6.48	7.49	7.09	6.17	1.85	0.57	3.00	0.20	7.90	6.03	5.39	4.88												
Na ₂ O	5.19	5.99	5.20	5.88	3.61	3.85	3.79	3.87	3.85	3.45	3.44	3.48	3.18	3.29	3.69	7.30	6.32	4.00	0.60	7.50	3.90	3.90	5.56												
K ₂ O	0.69	0.42	1.64	1.59	1.31	1.89	1.10	1.17	1.22	1.65	1.46	1.33	1.11	1.78	1.93	0.14	2.35	2.10	0.20	5.60	0.10	0.71	1.20												
P ₂ O ₅	0.32	0.31	0.15	0.28	0.23	0.20	0.28	0.26	0.25	0.26	0.32	0.25	0.21	0.24	0.22	0.04	0.30	0.00	0.00	0.00	0.00	0.00	0.00	0.00	0.00	0.00	0.00	0.00	0.00	0.00	0.00	0.00			
LOI	1.07	0.33	2.62	1.60	0.85	1.91	1.16	0.82	0.98	0.55	1.20	1.10	1.20	1.00	0.90	1.80	1.00	1.00	1.00	1.00	1.00	1.00	1.00	1.00	1.00	1.00	1.00	1.00	1.00	1.00	1.00				
Total	99.00	98.79	99.16	91.22	98.93	98.79	98.96	99.09	98.98	99.04	99.13	98.66	99.29	99.35	99.77	99.99	99.99	99.99	99.99	99.99	99.99	99.99	99.99	99.99	99.99	99.99	99.99	99.99	99.99	99.99					
Sc (ppm)	18	9	7	7	14	12	16	16	16	11	11	11	23	15	11	1	1	1	1	1	1	1	1	1	1	1	1	1	1	1					
V	132	68	40	—	116	120	126	125	117	116	121	126	209	142	102	—	—	—	—	—	—	—	—	—	—	—	—	—	—	—	—				
Cr	—	—	—	—	—	—	—	—	—	—	—	—	—	—	—	—	—	—	—	—	—	—	—	—	—	—	—	—	—	—	—				
Co	—	—	—	—	—	—	—	—	—	—	—	—	—	—	—	—	—	—	—	—	—	—	—	—	—	—	—	—	—	—	—				
Ni	33	3	2	—	3	9	3	3	3	3	2	2	2	1	2	1	2	1	2	1	2	1	2	1	2	1	2	1	2	1	2				
Cs	—	—	—	—	—	2	—	—	—	—	—	—	—	—	—	—	—	—	—	—	—	—	—	—	—	—	—	—	—	—	—				
Rb	14	8	31	43	47	69	38	34	44	59	60	46	61	58	63	622	556	115	53	39	200	200	150	102	492	97	97	97	97	97	97	97	97	97	
Sr	672	718	693	526	603	601	643	607	523	663	614	538	622	605	24	773	326	1	658	120	198	174	174	174	174	174	174	174	174	174					
Ba	294	261	504	672	313	394	256	263	268	323	399	377	307	412	405	24	14	15	15	15	9	3	21	14	14	14	14	14	14	14	14				
Nb	11	12	10	6	6	5	5	5	5	4	4	4	4	4	4	4	4	4	4	4	4	4	4	4	4	4	4	4	4	4	4				
Zr	194	239	240	165	137	147	124	117	127	173	172	131	140	148	157	110	138	141	66	227	103	61	117	117	117	117	117	117	117	117					
Hf	5	—	—	4	4	4	3	3	4	4	4	4	4	4	4	4	4	4	4	4	4	4	4	4	4	4	4	4	4	4	4				
Y	19	21	23	22	21	18	21	20	20	24	21	20	25	21	22	22	11	18	24	16	35	10	19	19	19	19	19	19	19	19					
La	17.5	25.2	29.6	15.0	18.8	17.1	16.0	15.3	17.3	21.7	13.1	17.9	14.7	18.7	19.1	10.5	19.4	16.0	<1	45.0	10.0	4.6	16.8	16.8	16.8	16.8	16.8	16.8	16.8	16.8					
Ce	39.6	56.9	62.8	38.4	41.4	44.5	36.9	34.1	39.4	42.1	29.6	40.0	34.5	39.9	45.8	22.4	49.9	43.0	19.0	73.0	21.1	9.8	33.0	33.0	33.0	33.0	33.0	33.0	33.0	33.0	33.0				
Pr	5.1	—	5.0	5.2	—	4.6	4.3	5.0	5.0	—	4.9	5.3	4.5	5.0	5.6	2.5	5.6	—	—	—	—	—	—	—	—	—	—	—	—	—	—	—	—		
Nd	22.3	27.6	24.4	22.3	21.0	<22	21.5	18.1	22.2	<22	18.9	23.1	19.3	22.0	24.8	8.6	18.8	—	—	—	—	—	—	—	—	—	—	—	—	—	—	—	—	—	
Sm	4.3	—	—	4.6	4.3	—	4.3	4.0	4.2	—	3.8	4.5	4.5	4.6	4.6	5.0	1.7	3.4	—	—	—	—	—	—	—	—	—	—	—	—	—	—	—	—	
Eu	1.28	—	—	1.24	1.27	—	1.45	1.23	1.25	—	1.32	1.18	1.26	1.13	1.23	0.22	0.69	—	—	—	—	—	—	—	—	—	—	—	—	—	—	—	—	—	
Gd	3.17	—	—	3.45	3.09	—	3.41	3.26	3.29	—	4.02	4.51	4.98	3.88	4.18	1.41	2.64	—	—	—	—	—	—	—	—	—	—	—	—	—	—	—	—	—	
Tb	0.55	—	—	0.67	0.66	—	0.72	0.61	0.64	—	0.55	0.54	0.72	0.6	0.68	0.25	0.48	—	—	—	—	—	—	—	—	—	—	—	—	—	—	—	—	—	
Dy	3.52	—	—	3.57	3.57	—	3.99	3.41	3.46	—	3.28	3.18	4.18	3.56	3.9	2.67	—	—	—	—	—	—	—	—	—	—	—	—	—	—	—	—	—	—	
Ho	0.62	—	—	0.63	0.63	—	0.79	0.63	0.79	—	0.66	0.63	0.8	0.68	0.8	0.33	0.6	—	—	—	—	—	—	—	—	—	—	—	—	—	—	—	—	—	—
Er	1.81	—	—	1.81	2.00	—	1.99	1.76	1.76	—	2.22	1.92	2.22	2.05	2.05	0.99	1.63	—	—	—	—	—	—	—	—	—	—	—	—	—	—	—	—	—	—
Tm	0.3	—	—	0.31	0.37	—	0.32	—	0.28	—	0.29	0.24	0.32	0.27	0.31	0.21	0.28	—	—	—	—	—	—	—	—	—	—	—	—	—	—	—	—	—	—
Yb	1.72	—	—	1.88	1.95</td																														

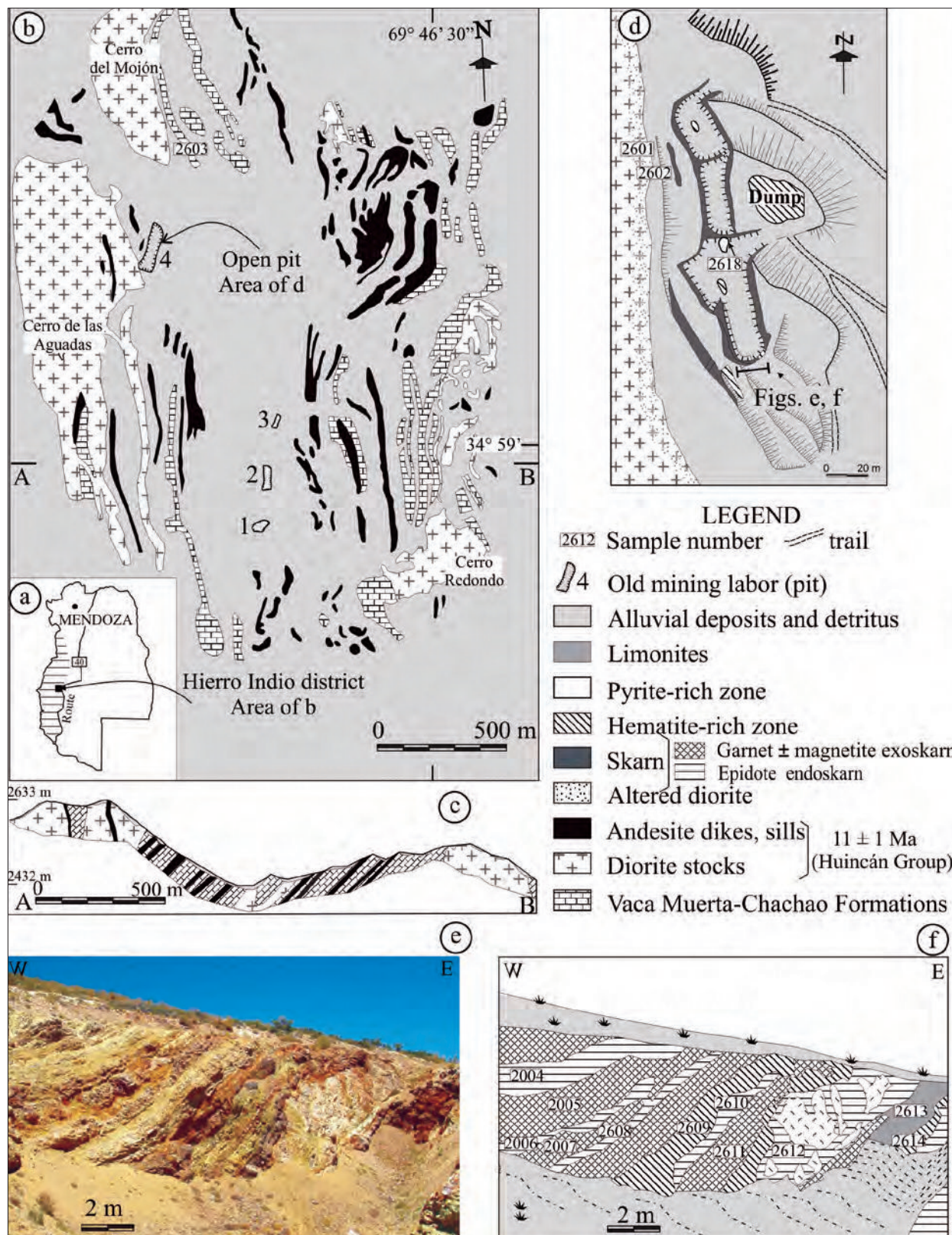


Fig. 4. Geology and alteration of the Hierro Indio Fe skarn. **a.** Location of the Hierro Indio Fe skarn in the thrust belt of Malargüe. **b.** Map of the Hierro Indio district showing geology and old mine workings. **c.** Schematic cross section showing the geology of the district. **d.** Alteration and mineralization in number 4 open pit. **e.** Photograph of the southernmost wall of number 4 open pit. **f.** Line diagram of area shown in (e) showing skarn mineralogy and zonation.

$^{143}\text{Nd}/^{144}\text{Nd}$ ratios for the Vegas Peladas igneous rocks are consistent with a mantle source for these rocks without crustal contamination (unpub. data of J. Pons).

The age of the diorite stock associated with Las Choicas Cu-(Ag) mineralization is not well constrained. Two samples of the diorite stock were analyzed by K-Ar and Ar-Ar methods, but the samples were too altered (feldspars were altered to scapolite and albite) to yield meaningful results. The least-altered diorite is metaluminous and calc-alkaline, although their relatively high alkalinity is due to post-depositional hydrothermal albitization (Fig. 3a,c). Whole-rock REE analyses (Table 2) normalized to average chondrite abundances are shown in Figure 3f. The REE slope of the Las Choicas diorite sample 4861 fits the trace of the Miocene diorites associated with Fe skarns (Hierro Indio-El Kaiser igneous rocks and Vegas Peladas diorite, but the LREE and HREE concentrations in the other analyzed samples are markedly depleted. In contrast to upper Miocene diorites, the Las Choicas diorite has a significant positive Eu anomaly. If these are primary geochemical characteristics, then the parental magma of Las Choicas diorite is different from the upper Miocene diorites. The N-MORB-normalized trace element patterns (Fig. 3e) show positive Ta and Nb anomalies with respect to Th and Ce, and have high Ti; these features are uncommon in other Miocene diorites and in magmas derived from sub-arc mantle sources (Kay and Mpodozis, 2002).

Fe Skarn Deposits

The Hierro Indio Fe Skarn

The Hierro Indio Fe skarn ($34^{\circ}59' \text{S}$, $69^{\circ}47' \text{W}$; Figs. 1b, 3a,b) was mined from 1950 to 1970, with production of 71 000 t of 40% to 50% Fe ore (Angeletti, 1984; Zanettini, 1999). Iron mineralization is hosted in the Vaca Muerta and Chachao formations, which consist of gray to dark gray limestone with intercalations of calcareous siltstone. Several small Miocene plutons and numerous sills and dikes (Huincán Formation) intrude the Vaca Muerta-Chachao formations in the core of the main syncline structure (Fig. 4b,c) and are intimately associated with the Fe skarn.

The igneous stock and sills are metaluminous, and the presence of abundant amphibole and magnetite are typical features of I-type plutons. The stock and sills contain zoned plagioclase ($\text{Or}_{1-2} \text{Ab}_{53-66} \text{An}_{33-46}$; Table 3), brown magnesiohastingsite (Table 3) with colorless, relic clinopyroxene cores, and accessory magnetite, titanite, apatite, and zircon. $^{40}\text{Ar}/^{39}\text{Ar}$ step-heating of a plagioclase grain from a diorite (see sample location in Fig. 4d) defines a plateau age of 11 ± 1 Ma (Fig. 5). The high Na_2O (5.19–5.99 wt.%) and CaO (5.10–9.44 wt.%), low Fe_2O_3^T (1.67–3.76 wt.%), and variable MgO concentrations (0.9–3.8 wt.%; Table 2) may reflect sub-solidus alteration of magmatic feldspar, and calcic amphibole replacement of primary magnesiohastingsite, respectively.

Skarn mineralization is exposed in four areas of open pits, the largest of which, number four (Fig. 4b,d), had originally a total surface area of 45 000 m². Skarn is associated

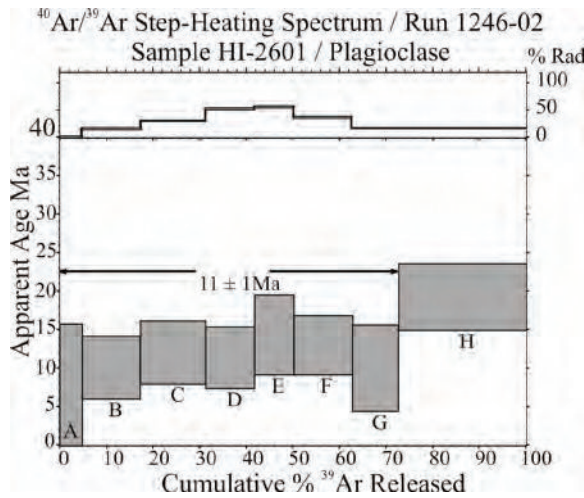


Fig. 5. $^{40}\text{Ar}/^{39}\text{Ar}$ step-heating spectrum of one plagioclase grain (1246-02) from the Hierro Indio diorite stock (sample 2601, see location in Fig. 4d). This sample has a plateau at 11 ± 1 Ma.

with andesite sills that intrude out from the roof of the main diorite pluton. The margins of the diorite stock and the sills near open pits have incipient alteration with actinolite \pm calcite \pm albite \pm titanite (<20 vol.%) and diopsidic pyroxene ($\text{Di}_{79-88} \text{Hd}_{11-21} \text{Jo}_{0.3-0.5}$; Table 3) \pm magnetite \pm apatite occurs as euhedral, fine-grained crystals. The hydrothermal magnetite contains less TiO_2 (2–4 wt.%) and Al_2O_3 (0.14–0.29 wt.%) than the coarser grained, magmatic magnetite (9–10 wt.% TiO_2 and 2–2.3 wt.% Al_2O_3).

In the southernmost walls of the number four pit, sills are replaced by massive epidote endoskarns with subordinate amphibole (green endoskarn; Figs. 4e,f, 6a). Massive epidote endoskarn also replaces the margin of the diorite stock in the northern pit. Limestone xenoliths, ovoid lenses up to 15 cm long, in the diorite are concentrically zoned from a calcite core, to epidote-actinolite, to a rim of clay (Fig. 6b). Both sills and endoskarns have been affected by intense supergene argillic alteration.

Limestone and siltstone of the Chachao Formation near altered sills have been replaced by brown, yellow brown, greenish brown exoskarns (0.5–3.0 m thick; Figs. 4e,f, 6c), and in the northernmost wall of number 4 pit they coalesce into one thick exoskarn body at the contact with the altered diorite stock. Garnet is the dominant prograde calc-silicate mineral (60–90 vol.%), with minor pyroxene and apatite. In thin section, garnet has a turbid appearance due to the presence of submicroscopic inclusions in cores and mid sections. Garnet crystals ($\text{Grs}_{3-66} \text{Adr}_{32-96} \text{Sps-Alm}_{0.5-1.8}$; Fig. 7a) are zoned with andraditic yellow and isotropic bands alternating with more grossularitic colorless, aniso-

Table 3. Representative Electron Microprobe Analyses of Magmatic Plagioclase and Amphibole, Hydrothermal Pyroxene, Amphibole, and Apatite in the Hierro Indio Fe Skarn

Plagioclase (wt.%)	Sample: 2601				Sample: 2601				Sample: 2601				Sample: 2601				Sample: 2601				Apatite				
	Core	Mid section	Rim	(wt.%)	Diopsidic Pyroxene				(wt.%)				Magnesiohastingsite				Actinolite				(wt.%)				
SiO ₂	56.49	59.58	56.71	57.41	SiO ₂	49.57	48.89	53.53	53.69	SiO ₂	40.23	40.95	44.08	55.10	55.20	CaO	56.34	53.77	53.21	53.78	53.28				
TiO ₂	0.04	n.d.	0.04	n.d.	TiO ₂	1.02	1.26	0.84	0.59	TiO ₂	3.64	3.47	3.15	0.40	0.40	P ₂ O ₅	41.11	44.39	43.86	42.58	43.85				
Al ₂ O ₃	27.20	25.20	27.28	27.37	Al ₂ O ₃	4.54	5.73	0.84	0.59	Al ₂ O ₃	15.31	14.49	10.34	1.80	1.56	F	4.19	2.74	2.95	2.68	2.70				
CaO	9.54	6.88	9.32	8.76	CaO	23.59	22.66	24.88	25.73	CaO	11.90	11.90	11.43	11.40	11.60	C1	n.d.	0.15	0.19	n.d.	0.15				
MgO	0.19	0.01	0.02	0.01	MgO	14.32	14.88	15.41	16.29	MgO	14.10	14.14	15.48	19.60	19.80										
¹ Fe ₂ O ₃	0.55	0.19	0.25	0.22	² FeO	6.73	6.89	5.36	3.67	² FeO	11.23	11.53	10.95	7.70	7.70										
MnO	0.04	n.d.	0.02	0.02	MnO	0.17	0.10	0.12	0.11	MnO	0.04	0.09	0.18	0.51	0.40										
K ₂ O	0.19	0.16	0.37	0.36	K ₂ O	n.d.	0.05	0.02	0.02	K ₂ O	0.60	0.65	0.75	0.10	0.10										
Na ₂ O	6.18	7.51	6.30	6.47	Na ₂ O	0.31	0.43	0.55	0.37	Na ₂ O	2.23	2.23	2.16	0.65	0.69										
P ₂ O ₅	n.d.	n.d.	n.d.	n.d.	P ₂ O ₅	—	—	—	—	P ₂ O ₅	—	—	—	—	—										
F	—	—	—	—	F	—	—	—	—	F	—	—	—	—	—										
Total	100.26	99.88	100.30	100.61	Total	100.25	100.89	100.80	100.55	Total	99.27	99.45	98.50	97.26	97.45	Total	101.64	101.05	100.21	99.04	99.98				
<i>(Cations based on 32 oxygens)</i>																									
<i>(Cations based on 6 oxygens)</i>																									
<i>(Cations based on 23 oxygens)</i>																									
Si	10.13	10.67	10.17	10.24	Si	1.84	1.80	1.95	1.96	Si	5.71	5.81	6.27	7.67	7.67	Ca	22.53	23.14	23.05	23.29	23.22				
Al	5.75	5.32	5.77	5.76	Al	0.16	0.20	0.04	0.03	Al _{IV}	2.29	2.19	1.73	0.30	0.26	P	12.99	15.10	15.01	14.57	15.10				
Ti	0.01	0.00	0.01	0.00	Ti	0.03	0.03	0.02	0.02	Ti	0.39	0.37	0.34	0.04	0.04	C1	0.00	0.23	0.13	0.00	0.09				
Fe ³⁺	0.07	0.03	0.03	0.03	Fe ²⁺	0.21	0.21	0.16	0.11	Fe ²⁺	1.20	1.23	1.17	0.81	0.81										
Mg	0.05	0.00	0.00	0.00	Mg	0.79	0.82	0.84	0.88	Mg	2.98	2.99	3.28	4.07	4.10										
Mn	0.01	0.00	0.00	0.00	Mn	0.01	0.00	0.00	0.00	Mn	0.00	0.01	0.02	0.06	0.05										
Ca	1.83	1.32	1.79	1.67	Ca	0.94	0.90	0.97	1.00	Ca	1.81	1.81	1.74	1.70	1.73										
Na	2.15	2.61	2.19	2.24	Na	0.02	0.03	0.04	0.03	Na	0.61	0.61	0.59	0.18	0.19										
K	0.04	0.04	0.08	0.08	K	0.00	0.00	0.00	0.00	K	0.11	0.12	0.14	0.02	0.02										
Orthoclase	1.1	0.9	2.1	2.0	Johannsenite	0.53	0.31	0.38	0.33	Mg(Mg+Fe)	0.71	0.71	0.74	0.83	0.84										
Albite	53.4	65.8	53.9	56.0	Diopside	78.70	79.12	83.36	88.48																
Anorthite	45.5	33.3	44.1	41.9	Hedenbergite	20.76	20.57	16.26	11.19																

Notes

¹All iron as Fe₂O₃.²All iron as FeO.

— = not analyzed; n.d. = not detected.

Pyroxene classification after Morimoto et al. (1988). Amphibole classification after Leake et al. (1997).

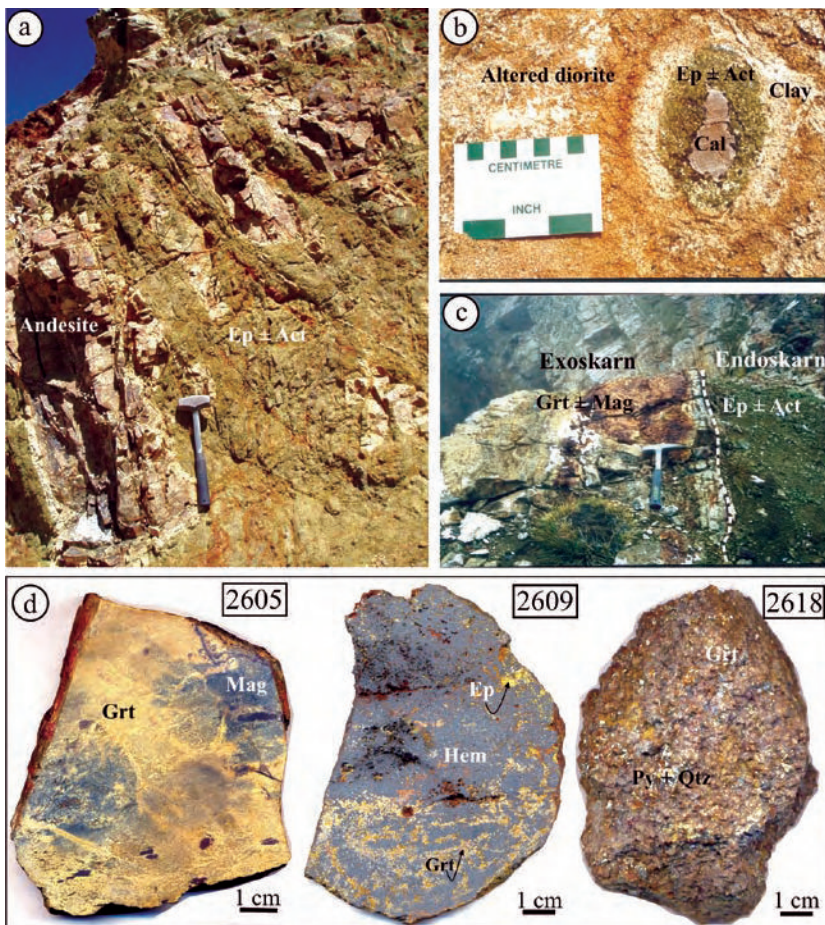


Fig. 6. Photographs of alteration styles in andesite, diorite, and limestone from the Hierro Indio Fe skarn. *a*. Massive epidote \pm amphibole endoskarn replacing andesite. *b*. Limestone xenolith in diorite replaced by calcite (core), epidote-vesuvianite (mid-section), and clay (rim). *c*. Contact between epidote endoskarn and garnet \pm magnetite exoskarn. *d*. Sample 2605: garnet \pm magnetite exoskarn with nodular texture; sample 2609: massive hematite zone associated with the epidote replacement of garnet; sample 2618: pyrite \pm quartz-rich pockets in the garnet exoskarn. Sample locations are shown in Fig. 4c,e. Abbreviations: Act = actinolite, Cal = calcite, Ep = epidote, Grt = garnet, Hem = hematite, Py = pyrite, Qtz = quartz (mineral symbols after Kretz, 1983).

tropic bands.

Garnet exoskarns contain very fine-grained, corroded clinopyroxene partially altered to chlorite and clays. Fluorine-rich apatite (2.68–4.12 wt.% F; Table 3) is scarce, but exhibits a widespread distribution in exoskarn, and occurs as very fine-grained prisms (0.05–0.10 mm) filling interstices between garnet. Retrograde alteration consists of biotite, chlorite, and epidote alteration of garnet, and interstitial quartz, calcite, and fibrous chalcedony. Fluid inclusions suitable for microthermometry were found only in late calcite from the garnet \pm magnetite exoskarn. Primary fluid inclusions in calcite are pseudo rectangular, range from 10 to 50 μm in size, and contain liquid water, vapor, and halite. First melting occurred at -65°C , indicating the presence of other cations in addition to Na^+ . The inclusions homogenized by vapor bubble disappearance over a temperature range of 190° to 250°C . Halite melting occurred between 199° and 270°C , corresponding to a calculated salinity range of 31 to 34 wt.% NaCl eq. (unpub. data of M. Franchini et al.).

Hypogene iron mineralization is comprised of magnetite, hematite, and, in distal exoskarn, minor pyrite. Magnetite associated with pyroxene and epidote in endoskarn is disseminated, whereas in garnet exoskarn magnetite also occurs as stringers, irregular aggregates, and bands that result in a banded and nodular texture (Fig. 6d, sample 2605). In distal exoskarns, hematite (0.5–5 mm) is the dominant oxide mineral and forms black, massive, and irregular bodies up to 4 m thick, some bounded by shear zones. Hematite rims relict garnet crystals that have been partially replaced by epidote (Fig. 6d, sample 2609). This replacement texture and the distal location of the hematite-rich zones, indicate that hematite postdates the deposition of garnet and magnetite, and is related to retrograde alteration.

Magnetite and hematite from Hierro Indio have low TiO_2 (0.02–0.10 wt.%) and contain no detectable Cr_2O_3 or V_2O_5 , typical of magnetite in skarn or low-grade metamorphic rocks (Sangster, 1969; Zürcher et al., 2001). These Fe oxides also contain less than 0.10 wt.% MnO, which is typical of magnetite in skarn deposits associated with gabbro and diorite in China (<0.3 wt.%; Xu and Zhang, 1998), Canada (0.1–0.17 wt.%; Sangster, 1969), Mexico (0.14 wt.%; Zürcher et al., 2001), and Senegal (≤ 0.036 wt.%; Schwartz and Melchor, 2004). These MnO concentrations are lower than the MnO concentrations of magnetite in skarns

associated with granite (0.38–0.93 wt.%; Xu and Zhang, 1998). Analyzed magnetite and hematite crystals have high concentrations of SiO_2 (0.3–5 wt.%) and CaO (0.1–1.5 wt.%), but it was not possible to determine whether inclusions of calc-silicate minerals account for the elevated SiO_2 and CaO concentrations or if the oxide minerals are enriched in these elements, as has been found in previous magnetite studies (Shiga, 1988; Westendorp et al., 1991). Figure 7b summarizes magnetite, and hematite compositions of the Hierro Indio skarn.

Pyrite is the only sulfide mineral in the Hierro Indio skarn, although traces of secondary copper minerals may indicate the likely presence of former hypogene Cu sulfides. Pyrite is abundant on the northern side of the southern pit, in a 5 m-thick outcrop (Fig. 4d, sample 2818). In this outcrop, pyrite occurs as euhedral crystals up to 1 cm in diameter with quartz, filling fractures and other permeable zones in the garnet \pm magnetite exoskarn, and locally forming pyrite \pm quartz-rich pockets (Fig. 6d, sample 2618).

The concentrations of major elements in endoskarn,

exoskarn, and unaltered protoliths are illustrated in Figure 8. The fresh limestone has 0.22 wt.% $\text{Fe}_2\text{O}_3^{(\text{total})}$. Diorite samples with incipient alteration also have low $\text{Fe}_2\text{O}_3^{(\text{total})}$ concentrations (3.1 and 1.67 wt.%). Endoskarn (sample 2610) in an andesite dike shows higher CaO concentrations than expected for this skarn zone due to the replacement of plagioclase by calcite accompanying epidote, which is also shown in the high loss on ignition (Fig. 8). SiO_2 , CaO , Al_2O_3 , MgO , and TiO_2 are negatively correlated with $\text{Fe}_2\text{O}_3^{(\text{total})}$ in protolith, endoskarn, and exoskarn samples corresponding to the progressive replacement of epidote ± calcite endoskarn and garnet ± magnetite exoskarn zones by distal hematite (epidote)-rich zones. Endoskarn and exoskarn samples are depleted in Na_2O and K_2O , and enriched in MnO and P_2O_5 compared to their protoliths. High Na_2O in diorite samples is due to albitization. MnO also shows a negative correlation with $\text{Fe}_2\text{O}_3^{(\text{total})}$, reflecting the replacement of epidote and garnet (minerals with MnO in endoskarn and exoskarn) by hematite in distal exoskarn zones. The enrichment in P_2O_5 correlates with the presence of interstitial apatite in association with prograde calc-silicates, a mineral that is depleted in samples with retrograde alteration ± pyrite (sample 2618) or supergene alteration of hematite-rich zones (sample 2614; Fig. 8; unpub. data of M. Franchini et al.).

The Vegas Peladas Fe Skarn

The Vegas Peladas iron deposit ($35^{\circ}20' \text{S}$, $69^{\circ}56' \text{W}$) is located 50 km NW of Malargüe (Fig. 9a). It is hosted in Jurassic marine sedimentary rocks of the Puchenque Formation that crop out on the northeast flank of Cerro De Las Minas, on both sides of Vegas Peladas creek (Fig. 9b). The Puchenque Formation consists of 500 m of alternating mudstone, wackestone rich in ammonites and pelecypods, and minor sandstone. Overlying this unit on the northeast side of the creek, are discontinuous gypsum outcrops of the Auquilco Formation. The sedimentary units are intruded by the following Neogene sequence: (1) a diorite-tonalite pluton; (2) a granodiorite pluton; (3) a granite pluton; and (4) andesite dikes and sills (Fig. 9b,c). The diorite-tonalite stock is the oldest unit in the area and is intruded by the granodiorite stock. Locally, the presence of abundant diorite-tonalite xenoliths (50 vol.%) within the granodiorite pluton, and textural evidence for plastic flow suggest that mingling occurred between the diorite-tonalite and granodiorite magmas. The granite pluton intrudes the diorite-tonalite and the granodiorite stocks with sharp contacts in the southeastern part of the district. In the northeastern zone, the contact of granite with the Puchenque Formation is concordant and caused hydraulic fracturing of the sedimentary rock, such that some fractures are filled with dikes and sills of rhyolite. Andesite dikes and sills have intruded all these igneous units. Rb-Sr isotopic analyses of whole rocks and biotite yielded an isochron age of 15.19 ± 0.24 Ma for granodiorite (sample VP27-E, Fig. 9b) (unpub. data of J. Pons). Fe skarns are associated with the diorite and granite plutons.

Fe Skarn Associated with Diorite: Diorite margins (Fig. 9c)

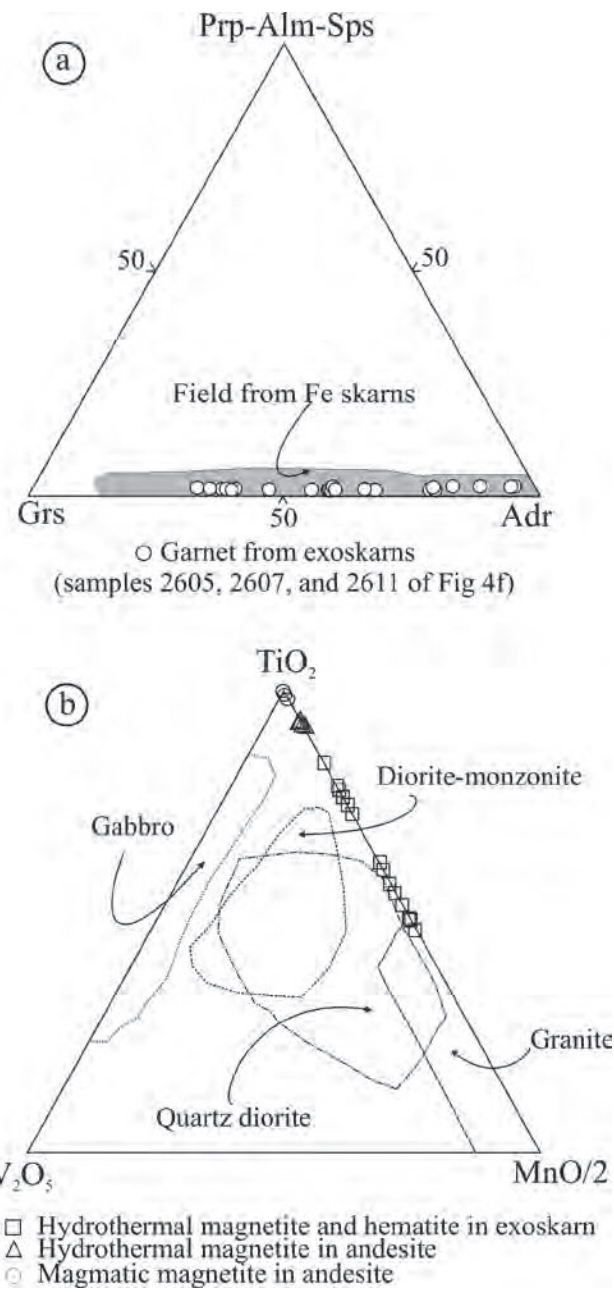


Fig. 7. **a.** Composition of garnet from the Hierro Indio exoskarn. The compositional field for garnet in Fe skarn deposits is shown for comparison (Meinert et al., 2005). **b.** Ternary V_2O_5 - TiO_2 - $\text{MnO}/2$ plot of magnetite and hematite from different alteration zones of the Hierro Indio Fe skarn; the compositional fields for magnetite in skarn deposits associated with various igneous rocks from China are shown for comparison (Xu and Zhang, 1998). Abbreviations: Adr = andradite, Alm = almandine, Grs = grossularite, Prp = pyrope, Sps = spessartine.

show incipient (10 vol.%) hydrothermal alteration, with mafic minerals replaced by amphibole ± chlorite ± calcite with magnetite ± titanite rims, plagioclase replaced by orthoclase ± epidote ± calcite patches, and magmatic magnetite with rims of titanite. On the contact with the sedimentary protoliths, the diorite stock is replaced by massive, greenish white, 0.2 to 0.5 m-thick quartz ± epidote ± amphibole

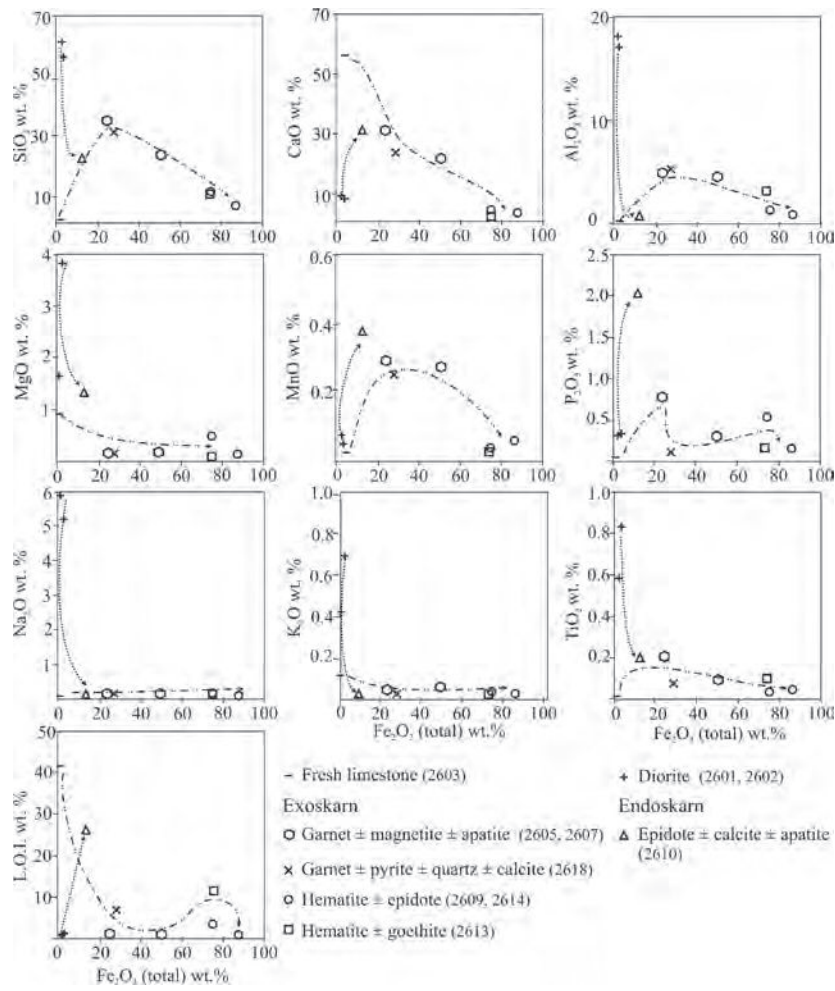


Fig. 8. Bivariate element plots showing SiO₂, CaO, Al₂O₃, MgO, MnO, TiO₂, Na₂O, K₂O, and L.O.I. vs. Fe₂O₃(total) for limestone, diorite, endoskarn, and exoskarn from the Hierro Indio prospect. Sample locations are shown in Fig. 4. The arrows indicate the different distribution patterns for endoskarn and exoskarn that reflect differences in protolith composition (marble vs. diorite) and in the metasomatic process.

endoskarn (Figs. 9c, 10). Limestone xenoliths in diorite are replaced by a brown garnet core partially replaced by epidote and an orthoclase rim with traces of quartz ± sericite. Dikes and sills that emanate from the diorite are mantled by thin (10–15 cm-wide), but massive epidote + calcite ± alkaline feldspar endoskarn envelopes (Fig. 11, sample VP24-H). Numerous veins, miarolitic cavities, and joints filled with quartz, magnetite, amphibole, epidote, alkaline feldspar, and pyrite cut the periphery of the diorite pluton (Figs. 10, 11, 12). Quartz + magnetite veins have an inner amphibole ± epidote and an outer alkali feldspar halo. Next to the contact with the granodiorite stock, the diorite is cut by veins of massive magnetite and locally by magnetite stockwork.

In the contact with altered diorite, mudstone, wackestone, and limestone have been transformed into quartz-feldspar-pyroxene-biotite-(sericite) banded hornfels rich in sulfides and Fr-Ti oxides (Figs. 9c, 10, samples 2693-5 and 2687; Fig. 12, sample 2651-A). The distribution of hornfels is controlled by the composition of the protolith.

The metamorphic aureole is approximately 800 m-wide (Fig. 9c). The exoskarn crops out along the southwestern margin of the creek, where it is 3 km long and has a maximum width of 54 m (Fig. 9c). This skarn is superimposed on hornfels as concordant bands and discordant veins with variable mineralogy, intensity, and distribution. The following zones were distinguished: (1) an inner brown garnet zone that grades laterally into (2) epidote + magnetite ± quartz zone; (3) an inner pyroxene + magnetite + quartz zone; (4) an intermediate garnet ± pyroxene zone; and (5) an external amphibole + mushketovite (magnetite pseudomorphs after hematite) + epidote ± calcite ± quartz zone that also overprints earlier alteration. The inner garnet zone (Fig. 10, sample 2684) is massive, reddish to yellowish brown, and the garnet contains abundant pyroxene and quartz inclusions. In thin section the garnet is zoned, with greenish isotropic and yellowish brown anisotropic concentric bands, and shows complex twins. The intermediate zone contains dark brown, isotropic garnet in textural equilibrium with clinopyroxene (Di_{24–50} Jo_{2–9} Hd_{74–41}; Fig. 13a). Garnet compositions become more Fe-rich from the inner zone (Adr_{52–82} Grs_{47–16} Alm-Sps_{1–2}), towards the intermediate zone (Adr_{96.2–100} Grs_{0.0–3.7} Alm-Sps_{0.0–0.08}; Fig. 13b).

Vapor-rich (>60 vol.% vapor) fluid inclusions coexist with saline (>50 vol.% solids) inclusions in quartz, garnet, and pyroxene from the prograde exoskarn (sample VP24-F, Fig. 11). Daughter crystals in saline inclusions are halite + sylvite ± hematite ± FeCl_n. Homogenization temperatures in garnet and pyroxene ranged from 550° to 670°C, and most salinities were in the range of 60 to 70 wt.% NaCl equiv. (Fig. 14). Preliminary isotopic measurements for water calculated to be in equilibrium with garnet from the inner exoskarn zone indicate δ¹⁸O values of 7.23‰ to 8.53‰ (unpub. data of J. Pons).

Retrograde alteration is superimposed on prograde exoskarn zones (Fig. 9c). This alteration consists of epidote ± quartz and epidote ± ferropargasite (Fig. 13c) ± quartz replacement of inner brown garnet and intermediate garnet ± pyroxene zones (Fig. 10, sample 2684; Fig. 11, samples VP19-U and VP24-F), and actinolite (Fig. 13c) ± epidote ± quartz envelopes of distal mushketovite veins (Fig. 10, sample 2642; Fig. 12, sample 2656-3). The latter assemblage extends outward into hornfels along joints and bedding planes where it replaces hornfels and exoskarn veins in hornfels. The latest alteration consists of widespread quartz

+ calcite ± chlorite ± titanite ± orthoclase ± pyrite filling open spaces and/or distal veins and patches that cut and replace earlier alteration (Fig. 10, sample 2693-5; Fig. 11, sample VP24-F; Fig. 12).

The main iron ores in the Vegas Peladas skarn consist of magnetite, specular hematite, and mushketovite. Magnetite is closely associated and in textural equilibrium with quartz and epidote in endoskarn and with pyroxene in exoskarn (Fig. 12, sample 2653-D), but the largest massive magnetite orebodies occur with epidote and quartz replacing prograde inner and intermediate garnet-rich exoskarn zones (Fig. 10, sample 2684). This massive magnetite contains between 87 and 92 wt.% $\text{Fe}_2\text{O}_3 + \text{FeO}$, with high SiO_2 , MgO , CaO , Na_2O , and K_2O due to calc-silicate mineral inclusions. Magnetite MnO content increases from core (below detection) to rim (0.22 wt.%; Table 4). Most of the specular hematite was precipitated late, during the retrograde alteration of prograde exoskarn (Fig. 11, sample VP24-F), and much of this specularite was later transformed into mushketovite. Thus, distal iron-rich orebodies consist of mushketovite with amphibole envelopes (Fig. 11, sample VP19-U; Fig. 12, sample 2656-3). Mushketovite has higher $\text{Fe}_2\text{O}_3 + \text{FeO}$ concentrations (98–99.5 wt.%) than early magnetite (Table 4). Both iron oxide minerals have low MnO (up to 0.22 wt.%), typical of magnetite from iron skarns associated with diorite-gabbro-diorite plutons (<0.3 wt.%; Xu and Zhang, 1998). Iron ore samples contain up to 240 ppm Cu with anomalous Ag concentrations in the distal mushketovite bodies (Table 5). Pyrite concentrations in the entire skarn average 1 vol.-%.

Fluid inclusions in quartz associated with retrograde mushketovite + epidote + quartz replacement of intermediate exoskarn (sample VP19-U, Fig. 11) have homogenization temperatures between 290° and 436°C, and salinities between 32 and 50 wt.% NaCl equiv. (Fig. 14). These fluid inclusions contain daughter crystals similar to those in the prograde exoskarn, and a crystal with reverse (retrograde) solubility that may be calcite. Calcite in late veins (sample 2642, Fig. 10) contains liquid-rich inclusions (averaging 92.5 vol.% liquid), which have the lowest homogenization temperatures (165°–315°C) and salinities (12–14 wt.% NaCl equiv.) of all measured inclusions (Fig. 14). Evidence for boiling was found in the retrograde stage. In quartz associated with retrograde mushketovite + epidote

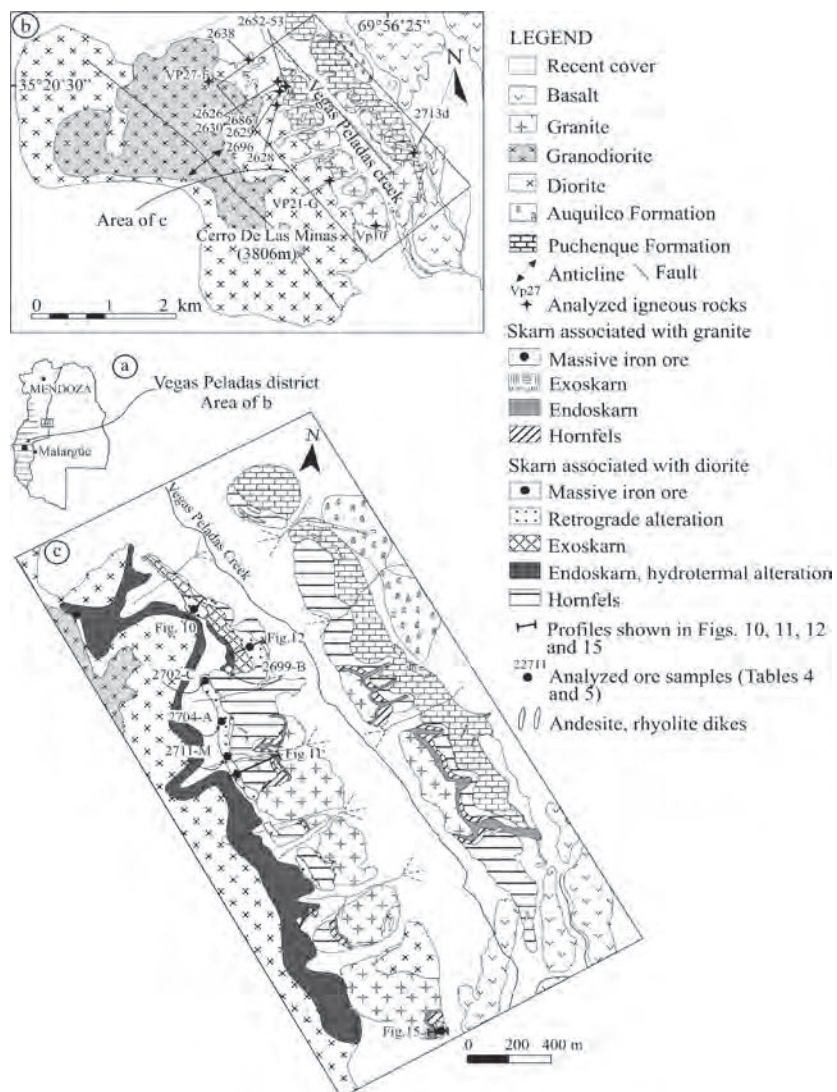


Fig. 9. *a*. Location of the Vegas Peladas Fe skarn in the thrust belt of Malargüe. *b*. Geologic map of the Vegas Peladas district with the location of analyzed igneous rocks shown in Table 2; the box indicates area of detailed mapping and sampling shown in *c*. *c*. Map of the investigated area showing geology, alteration, and mineralization and location of the profiles shown in Figs. 10–12 and 15, and the analyzed ore samples of Tables 4 and 5.

replacement of intermediate exoskarn (sample VP19-U, Fig. 11), pairs of spatially related saline inclusions (32–34 wt.% NaCl equiv.) and vapor-rich inclusions homogenized at the same temperature (420°C liquid, 420°C vapor), consistent with boiling. This boiling temperature correspond to a vapor pressure of 325 bars (Bodnar et al., 1985; unpub. data of J. Pons).

Iron Skarn Associated with the Granite Pluton: On the SE flank of Cerro de Las Minas Hill, a granite pluton, a rhyolite dike, and multiple sills have intruded marble and hornfels, forming a metamorphic aureole only few meters wide with pyroxene, scapolite, and amphibole hornfels, and a banded skarn (Figs. 9c, 15, sample 2709). Isotropic brown garnet ± quartz veins and vugs replace both granite and the rhyolite dike (Fig. 15, sample VP5), whereas in rhyolite

Table 4. Representative Electron Microprobe Analyses of Magnetite and Mushketovite from the Exoskarn Associated with Diorite in the Vegas Peladas District

Sample	2711M	2711M	2711M	2711M	2711M	2656-3	2656-3	2656-3	2656-3	2656-3	2656-3	2656-3	2656-3	2656-3	2656-3	2656-3	
						Magnetite											
	Magnetite					Mushketovite											
(wt.%)	1-core	1-rim	2-core	2-rim	3-core	1-core	1-rim	1-rim	2-core	2-rim	2-rim	3-core	3-rim	3-rim	4-core	4-rim	4-rim
SiO ₂	2.87	0.88	0.17	0.18	2.29	—	—	—	—	—	—	—	—	—	—	—	—
TiO ₂	0.00	0.00	0.00	0.06	0.04	0.04	0.04	0.04	0.04	0.03	0.05	0.02	0.02	0.00	0.01	0.01	0.04
Al ₂ O ₃	0.17	0.08	0.02	0.04	0.09	0.15	0.12	0.17	0.40	0.24	0.21	0.33	0.28	0.45	0.19	0.12	0.25
Fe ₂ O ₃	35.61	38.29	38.80	39.07	37.00	41.88	41.87	41.77	41.79	41.88	42.38	42.13	42.30	41.49	42.30	41.65	41.82
FeO	50.99	52.78	52.50	52.75	52.56	56.50	56.48	56.41	56.49	56.56	57.15	56.87	57.12	56.14	57.13	56.20	56.49
MnO	0.00	0.08	0.00	0.22	0.00	0.14	0.15	0.06	0.10	0.12	0.12	0.05	0.03	0.06	0.05	0.08	0.09
MgO	0.15	0.01	0.00	0.01	0.10	0.00	0.01	0.00	0.03	0.00	0.02	0.01	0.03	0.01	0.00	0.01	0.01
CaO	0.69	0.16	0.02	0.08	0.50	—	—	—	—	—	—	—	—	—	—	—	—
K ₂ O	0.10	0.04	0.01	0.01	0.08	—	—	—	—	—	—	—	—	—	—	—	—
Na ₂ O	0.16	0.00	0.01	0.01	0.07	—	—	—	—	—	—	—	—	—	—	—	—
ZnO	—	—	—	—	—	0.01	n.d.	0.09	n.d.	n.d.	0.03	0.01	n.d.	n.d.	0.01	0.02	0.02
NiO	0.01	n.d.	0.06	n.d.	n.d.	0.01	n.d.	n.d.	n.d.	n.d.	0.02	0.04	0.03	n.d.	n.d.	n.d.	0.01
CoO	—	—	—	—	—	n.d.	n.d.	0.01	0.01	n.d.	0.02	0.01	n.d.	0.07	0.03	n.d.	0.01
MoO ₃	—	—	—	—	—	n.d.	n.d.	0.03	n.d.	n.d.	n.d.	n.d.	n.d.	0.05	n.d.	n.d.	0.03
Cr ₂ O ₃	0.00	0.00	0.02	0.00	0.05	—	—	—	—	—	—	—	—	—	—	—	—
Total	90.74	92.32	91.61	92.43	89.06	94.53	94.48	94.38	94.69	94.64	95.75	95.25	95.57	94.10	95.49	93.92	94.59
(Cations based on 32 oxygens)																	
Si	1.32	0.42	0.08	0.08	1.04	0.00	0.00	0.00	0.00	0.00	0.00	0.00	0.00	0.00	0.00	0.00	0.00
Ti	0.00	0.00	0.00	0.01	0.01	0.01	0.01	0.01	0.01	0.01	0.01	0.00	0.00	0.00	0.00	0.00	0.01
Al	0.09	0.05	0.01	0.02	0.05	0.08	0.06	0.09	0.21	0.13	0.11	0.17	0.15	0.24	0.10	0.07	0.13
Fe ³⁺	14.21	15.41	15.89	15.87	14.57	15.94	15.95	15.93	15.85	15.91	15.91	15.88	15.90	15.84	15.93	15.95	15.90
Fe ²⁺	28.68	30.97	31.77	31.63	29.43	31.80	31.83	31.79	31.61	31.75	31.72	31.65	31.71	31.56	31.82	31.86	31.71
Mn	0.00	0.03	0.00	0.09	0.00	0.05	0.06	0.02	0.04	0.04	0.04	0.02	0.01	0.02	0.02	0.03	0.03
Mg	0.10	0.01	0.00	0.01	0.07	0.00	0.00	0.00	0.02	0.00	0.01	0.01	0.02	0.01	0.00	0.00	0.01
Ca	0.34	0.08	0.01	0.04	0.25	0.00	0.00	0.00	0.00	0.00	0.00	0.00	0.00	0.00	0.00	0.00	0.00
Na	0.14	0.00	0.01	0.01	0.06	0.00	0.00	0.00	0.00	0.00	0.00	0.00	0.00	0.00	0.00	0.00	0.00
K	0.06	0.02	0.01	0.01	0.04	0.00	0.00	0.00	0.00	0.00	0.00	0.00	0.00	0.00	0.00	0.00	0.00
Zn	0.00	0.00	0.00	0.00	0.00	0.00	0.00	0.03	0.00	0.00	0.01	0.00	0.00	0.00	0.01	0.01	0.01

*Notes*Fe³⁺/Fe²⁺ calculated according to Droop (1987).

— = not analyzed; n.d. = not detected.

sills the alteration consists of scapolite (Me_{28–36}) ± albite ± pyroxene with envelopes of green pyroxene (Fig. 15, sample VP1). Near endoskarn, marble is replaced by a zoned exoskarn with an inner brown garnet ± pyroxene ± quartz zone (Fig. 15, samples 2711-I and VP1) and an outer green garnet (Adr_{30–81} Grs_{69–19} Alm-Sps_{0.6–0.1}; Fig. 13b) + pyroxene (Di_{82–92} Jo_{4–3} Hd_{14–5}; Fig. 13a) zone (Fig. 15, sample 2711-I), whereas hornfels is replaced by scapolite ± pyroxene (Hd_{74–94}; Fig. 15; sample 2709).

Fluid inclusions in quartz from the inner garnet + pyroxene + quartz zone are multiphase (with halite ± sylvite ± opaque daughter minerals) and coexist with vapor-rich inclusions. Homogenization temperatures range from 340° to 560°C, and salinities are between 30 and 45 wt.% NaCl

equiv. (Fig. 13; unpub. data of J. Pons).

Late ferroactinolite (Fig. 13c) ± scapolite (Me_{25–30}) ± pyrite veins cut exoskarn and marble (Fig. 15, sample 2709). A few small magnetite bodies are associated with this alteration. The largest outcrop (1.5 × 6 m) contains mushketovite and mushketovite ± calcite lenses and veins cutting the garnet endoskarn hosted in the rhyolite dike (Fig. 15, sample VP5). Another Fe mineralized zone is located in marble, as lenses of specular hematite and next to the rhyolite dike, as lenses of mushketovite (Fig. 15). In the northeastern creek margin, scapolite ± green garnet ± pyroxene exoskarn replaces the sedimentary protolith in the contact with rhyolite dikes and sills, which lack endoskarn or mineralization. Late chlorite ± calcite ± pyrite ± epidote

and quartz ± calcite ± pyrite veins cut the earlier alteration (Fig. 15, samples VP6, VP5, and 2711-I).

Las Choicas Prospect (34°54'55"S, 70°16'40"W)

Las Choicas with 13 other Cu prospects in the Valle Hermoso district is the largest Cu concentration known in southwest Mendoza province (estimated 30 Mt with 1.5% Cu and 20 g/t Ag contained in eight prospects). The mine is located at 3200 m elevation near the international border with Chile and 47 km west of the Las Lefias ski center (Fig. 16a). From 1902 to 1927, the company Mining Exploration Limited operated in the area and discovered the Atalaya and Choiquitas veins and several other prospects located to the south and east of Las Choicas. Between 1937 and 1940, the mining company Valle Hermoso from Chile explored the district and operated the Las Choicas mine via three N-S-striking adits: at 3107 m (200 m long), at 3142 m (190 m long) located 8 m below a rich ore shoot developed between diorite and calcareous sandstone, and at 3170 m (140 m long) where it connected with a pit exploiting the uppermost outcrops (3190 m; Fig. 16c). The company extracted high-grade ore (20% Cu and 100–400 g/t Ag) that was transported to Chile.

Five decades later (1994–1998) Cominor Ingenieros y Proyectos S.A. mapped the Valle Hermoso district at a scale of 1:25 000 and the main prospects at a scale of 1:2000. They defined two main types of mineralization: Las Choicas-type irregular bornite-chalco-pyrite bodies at the contact of the La Manga Formation with a diorite pluton; and Tordillo-type stockwork veinlet, veins, and breccias hosted in the volcanic and volcaniclastic facies of the Tordillo Formation (Cominor Ingenieros y Proyectos S.A., 1999). Figure 16b shows the location of the Las Choicas-type prospects and six of the nine Tordillo-type prospects located northwest of Las Choicas (Aguila prospect) and 6 km to the east, extending from Amelia to 33 km south of Amelia. Thus, the area containing both deposit types is more than 300 km².

The company conducted induced polarization and magnetic surveys in the manto-type El Burrero and in Las Choicas-Atalaya prospects, respectively (Cominor Ingenieros y Proyectos S.A., 1999). Results of these studies were the basis for drilling holes located in Las Choicas-Atalaya prospects with a total length of 3859 m. Unfortunately there was not a good correlation between

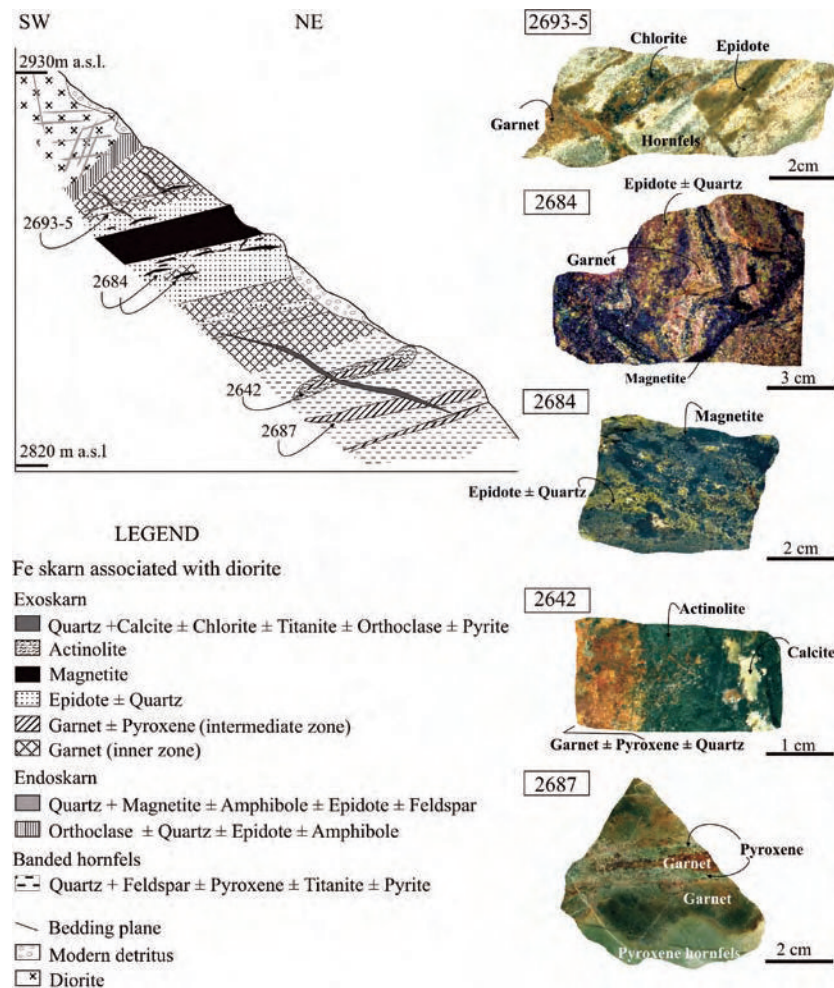


Fig. 10. Schematic SW-NE profile of the Fe skarn associated with diorite shown in Fig. 9c, including photographs of the main alteration and mineralization styles in the profile. Sample 2693-5: joints control the garnet exoskarn distribution in pyroxene hornfels and its late retrograde alteration to epidote ± chlorite. Sample 2684: retrograde magnetite ± epidote ± quartz zone of proximal garnet exoskarn. Sample 2642: intermediate garnet ± pyroxene exoskarn replaced by amphiboles and late calcite. Sample 2687: intermediate garnet ± pyroxene exoskarn zone cut pyroxene hornfels.

clear anomalies detected below and west of the mineralized structures and drilling results. The estimated resource of 400 000 t with 4.27% Cu and 30 g/t Ag for Las Choicas is open to the north (Coloso prospect). The Atalaya prospect has been incompletely explored by drilling holes and remains prospective. Aguila and other Tordillo-type prospects have significant exploration potential considering their widespread occurrence in the district, and geological and mineralogical similarities with high-grade manto-type Chilean Cu deposits (Cominor Ingenieros y Proyectos S.A., 1999).

Local Geology

The major topographic features in the district are two regional folds that run almost parallel to the international border for about 100 km. The Las Choicas mine is located in the apex of the western fold that consists of a 015°-trending anticline cut by post-mineralization faults trending 120°, and a series of postglaciation faults (Fig. 16b).

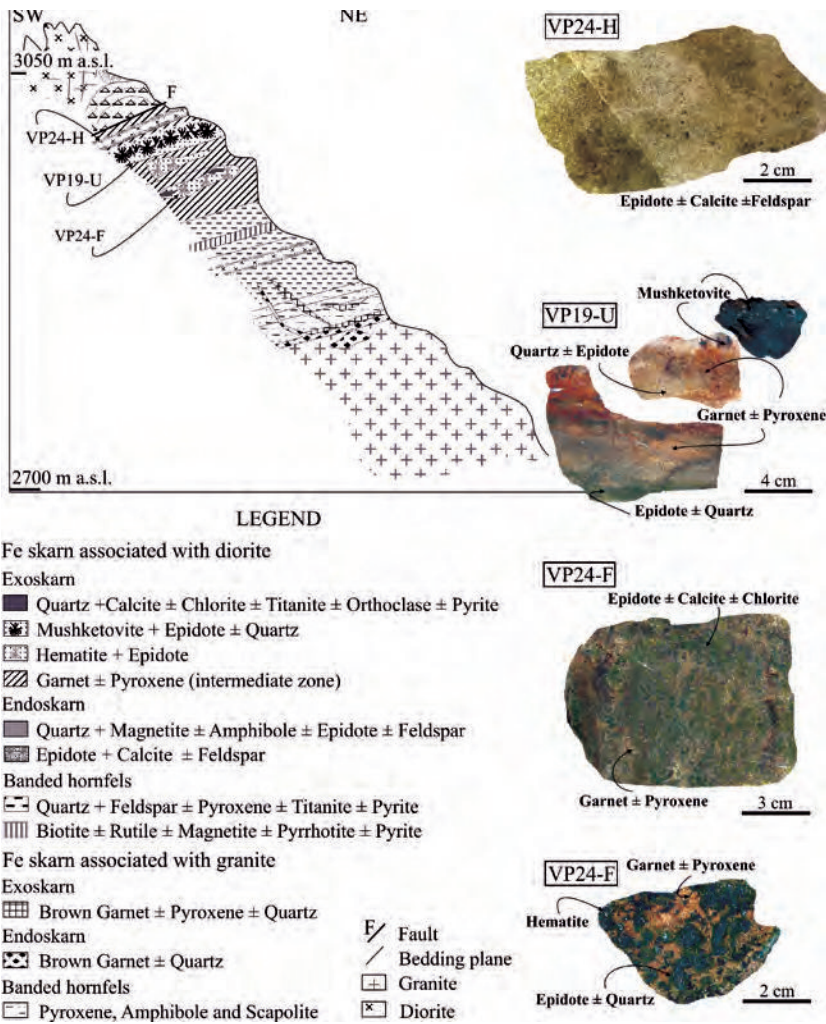


Fig. 11. Schematic SW-NE profile of the Fe skarn associated with diorite and skarn associated with granite shown in Fig. 9c, including photographs of the main alteration and mineralization styles in the profile. Sample VP24-H: epidote + calcite ± alkali feldspar endoskarn envelope replacing a diorite dike. Sample VP19-U: intermediate garnet ± pyroxene exoskarn partially altered to epidote ± quartz and distal mushketovite. Sample VP24-F: intermediate garnet ± pyroxene exoskarn partially replaced by specular hematite clots rimmed by epidote ± quartz and late calcite ± chlorite.

Sedimentary rocks in the region include the Jurassic Lotena-Chacay Group and the Late Jurassic–Early Cretaceous Mendoza Group (Fig. 16b). The La Manga Formation, the oldest unit in the area of the Lotena Chacay Group, has been particularly affected by hydrothermal alteration and mineralization. Its upper member hosts the Las Choicas mine and other prospects with barite veins and Cu-Ag mineralization (Fig. 16b). Overlying the La Manga Formation are evaporites of the Auquilco Formation, with discontinuous outcrops mostly restricted to dolines within moraine deposits in the valley of Las Choicas creek. Capping these shallow water sequences is the continental Tordillo Formation (upper Kimmeridgian), represented by two facies: red sandstone intercalated with thick volcanic and volcaniclastic rocks, and volcanic breccias.

Granodiorite plutons that have been assigned to the Miocene due to their similarities with the nearby Chilean Miocene plutons (Cominor Ingenieros y Proyectos

S.A., 1999) crop out north of the Las Choicas anticline, in Paso Las Damas, the international pass to Chile. Of special interest for Las Choicas-type Cu mineralization is a series of igneous outcrops in the La Manga Formation (Fig. 16b). These consist of small diorite bodies that have been described as “Choicas diorite”, and several dikes of similar composition that are probably apophyses of an unexposed intrusive stock. The biggest exposure is in the Las Choicas mine, and consists of an elliptical body 450 m long with abundant prismatic plagioclase crystals. The chemical composition of least-altered diorite is presented in Table 2 and in Figure 3a–h.

Alteration and Mineralization

The old underground workings are no longer accessible. Based on old maps and sections of Las Choicas (Devito, 1954; Angellelli, 1984), known copper mineralization occurs in an irregular zone with the same orientation as the anticline axis (N20°E) and dips 50° W. Mineralization occurs along lithological contacts between diorite apophyses and the clastic and calcareous sedimentary rocks of the La Manga Formation. In particular, the calcareous members of this formation host high-grade ore shoots (Fig. 17). The main mineralized body is 220 m long, ranges in thickness from 6 to 20 m, reaches a depth of 150 m in its southernmost extreme, and contains ore shoots between weakly mineralized zones. In addition, the numerous small mineralized diorite outcrops

nearby suggest the presence of a blind igneous body at depth, which may increase the potential of the mine. Samples from outcrops and old dumps permitted study of the alteration and mineralization.

In the uppermost levels (3250 m), sills in the La Manga Formation have a porphyritic texture and show moderate chlorite ± carbonate replacement of the ground mass and plagioclase phenocrysts, whereas pyroxene and magnetite remain fresh. The sills contain Cu sulfides (2 vol.%) as chalcocite partially replaced by covellite associated with alteration and late albite veinlets. Alteration of the diorite outcrops (20–30 vol. % of rock; samples 4856 and 4861, Table 2) near old mine workings (~150 m) consists of chlorite + calcite ± albite ± ilmenite ± apatite. Chlorite + calcite and traces of fibrous amphibole occur as pseudomorphic replacement of clinopyroxene. Chlorite replaces plagioclase as fine clots and fills interstices. Albite rims plagioclase and fills microveinlets with calcite. Ilmenite

occurs as fine-grained, euhedral prismatic crystals near altered mafic minerals. Locally there are clots up to 2 cm wide that contain relict garnet with patches of epidote, both surrounded by chlorite + calcite ± quartz ± pyrite.

In the 3142 m elevation adit, incipient brecciation is represented by the assemblage chlorite + calcite ± apatite ± titanite, which has invaded the matrix and clasts of the lowermost tuffaceous sandstone and siltstone units through fractures, locally resulting in a fragmental appearance without significant fragment displacement. The primary components of the protolith are replaced by fine-grained calcite ± titanite ± apatite with local chlorite. Small- to medium-size angular fragments are cut by numerous microfractures and some have been dislocated and replaced by the hydrothermal infill of calcite ± chalcopyrite ± quartz with rare sphalerite (Fig. 18). This brecciation stage marks the introduction of Cu mineralization (1.7% Cu, Table 6).

Intensely altered diorite is present in the 3170 m elevation adit and in samples from the mine dumps, such as the dark green, fine-grained areas of samples 4865-B, -C, and -D (Fig. 19) in which the mafic components have been replaced by chlorite (magnesian chamosite; Table 7) ± calcite ± titanite and a calcic amphibole rim (magnesiohornbende; Table 7); some samples contain relict biotite. Plagioclase is turbid and variably altered to phyllosilicates, scapolite, or is rimmed by hydrothermal albite (Table 7); titanite ± leucoxene have pseudomorphically replaced ilmenite. Prismatic aggregates of apatite (Table 7) are widespread. Bornite with subordinate chalcopyrite and minor millerite (Table 8) occurs as clots up to 2 cm in diameter, vugs, and several stages of veins and fine veinlets with calcite + albite ± quartz envelopes (Fig. 19). Bornite and chalcopyrite exhibit supergene alteration to digenite ± covellite along microfractures and/or grain boundaries. Altered diorite contains high Cu (4–10 wt.%), Ni (0.3–0.4 wt.%), and Cr (153–275 ppm; Table 6). Similar alteration and mineralization in the sedimentary protoliths (samples 4865-F, -E, -G, and -I; Fig. 19) cut a thin prehnite (Table 7) envelope at the con-

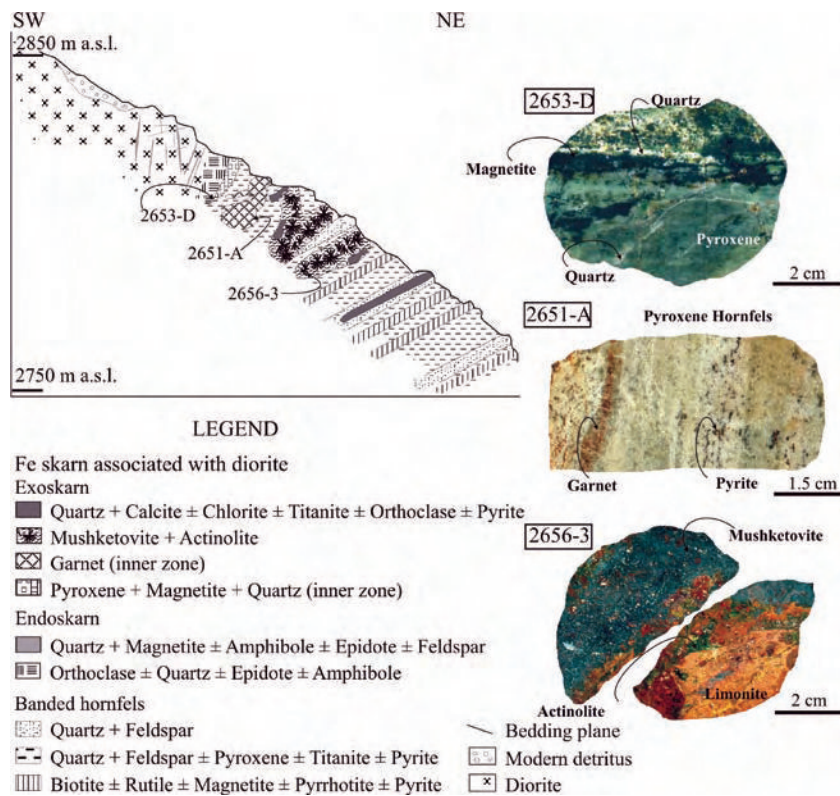


Fig. 12. Schematic SW-NE profile of the Fe skarn associated with diorite shown in Fig. 9c, including photographs of the main alteration and mineralization styles in the profile. Sample 2653-D: inner pyroxene ± magnetite exoskarn. Sample 2651-A: garnet exoskarn vein cutting pyroxene hornfels. Sample 2656-3: distal, partially oxidized, mushketovite veins with ferroactinolite ± Mg-hornblende envelopes.

Table 5. Geochemistry of Iron Ore Samples from the Skarn Associated with Diorite in the Vegas Peladas District

Sample	2684	2656-3	2699-A	2699-B	2702-C	2704-A	2711-M
Location	Fig. 9	Fig. 10	Fig. 8c				
<i>(wt.%)</i>							
Al	0.21	0.07	0.17	0.17	0.40	0.04	0.13
Fe	50.15	54.64	33.45	14.26	60.23	42.94	30.94
Mn	0.04	0.06	0.02	0.01	0.12	0.11	0.05
Mg	0.06	0.03	0.10	0.05	0.07	0.01	<0.010
Ca	0.92	0.28	0.11	0.10	0.37	1.92	10.09
Na	0.03	0.07	0.01	0.01	0.03	0.01	0.02
K	0.09	0.06	0.03	0.03	0.04	0.02	0.01
P	0.03	0.01	0.04	0.02	0.01	0.02	0.00
Co	0.00	0.00	0.00	0.00	<0.001	<0.001	<0.001
Ni	0.00	<0.001	0.00	<0.001	0.00	0.00	<0.001
Cu	<0.001	0.02	<0.001	<0.001	0.00	<0.001	<0.001
Sr	0.00	0.00	0.00	0.00	0.00	0.00	0.00
Pb	<0.010	<0.010	0.02	<0.010	<0.010	<0.010	<0.010
Sb	<0.001	<0.001	0.00	<0.001	0.00	<0.001	<0.001
W	0.00	0.02	0.04	0.02	0.03	<0.001	0.00
<i>(g/t)</i>							
Ag	<0.300	2.90	0.50	<0.300	<0.300	<0.300	0.70
Au	<0.010	0.02	<0.010	<0.010	0.02	0.02	<0.010

Notes

Elements analyses of iron ore samples were by ICP, and for Au by fire assay, at Acme Analytical Laboratories, Canada. Cr (<0.001 wt.%), Zn (<0.010 wt.%), As (<0.010 wt.%), Mo (<0.0010 wt.%), Cd (<0.001 wt.%), Hg (<0.001 wt.%), and Bi (<0.010 wt.%) below detection.

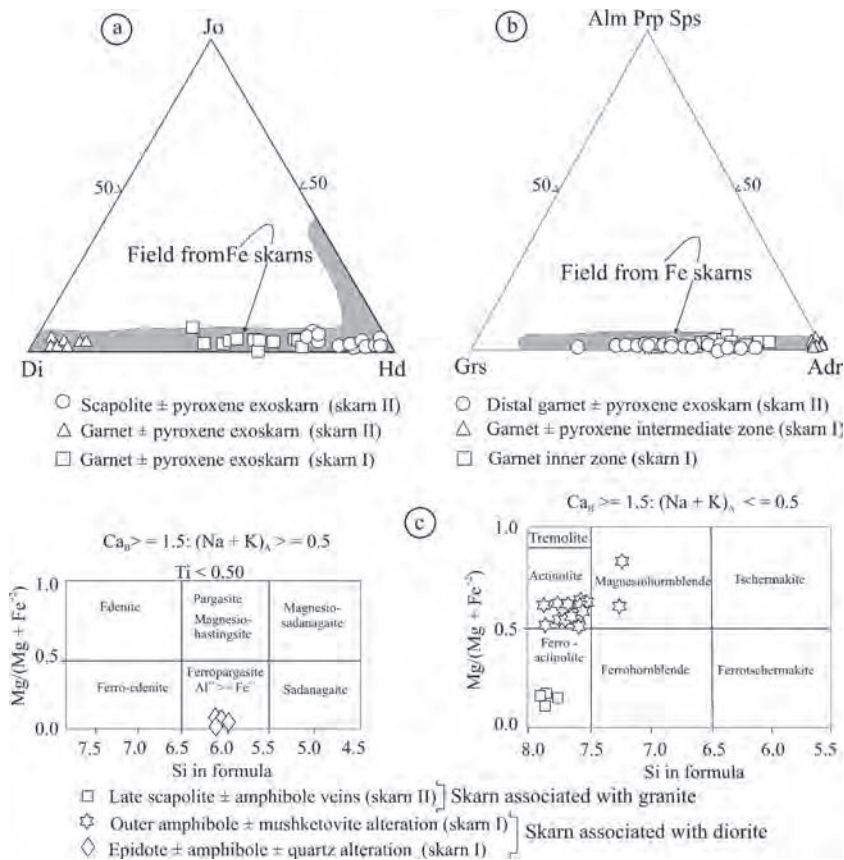


Fig. 13. *a*. Composition of pyroxene from the Vegas Peladas exoskarns associated with diorite and granite. *b*. Composition of garnet from the Vegas Peladas exoskarns associated with diorite (skarn I) and granite (skarn II). The compositional fields for pyroxene and garnet in Fe skarn deposits (Meinert et al., 2005) are shown in both diagrams for comparison. *c*. Composition of amphibole from the Vegas Peladas retrograde alteration stages associated with diorite and granite.

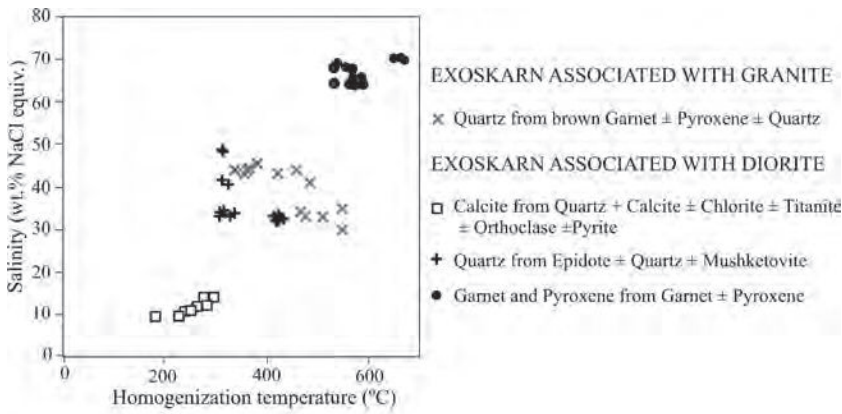


Fig. 14. Salinity versus homogenization temperature diagram for Vegas Peladas prograde and retrograde alteration assemblages in Fe skarns associated with diorite and granite. See text for explanation.

tact with altered diorite (samples 4865-F and -I; Fig. 19), and contain similar Cu grades and locally anomalous Zn (440 ppm), As (538 ppm), Mo (79 ppm), Ag (48 ppm), and U (133 ppm; Table 6). The bornite-chalcopyrite mineralization grades outwards to pyrite-rich zones that contain high Co (355 ppm; Table 6; Fig. 19, sample 4865-H).

In the upper parts of the old workings, at 3190 m elevation, a 2 m-wide bornite ± chalcocite ± malachite vein network occurs in diorite at the contact with the clastic member of La Manga Formation (Fig. 20). The network is controlled by two main joint orientations striking 080° and dipping 72°N and 20°N, and a third joint set that is N–S and near vertical. This zone contains high Cu (10 wt.%) and Ag (324 ppm; Table 6). In the walls of the network, the diorite is altered to chlorite ± white mica ± titanite ± leucoxene (sample 4860-A, Fig. 20), whereas siltstone and calcilutite at the contact with the altered diorite (samples 4860-B, 4864-A, 4864-B; Fig. 20) have euhedral and coarser grained titanite accompanying albite ± calcite ± chlorite ± apatite patches, and exhibit zonation in sulfide mineralogy from innermost bornite veins to distal chalcopyrite ± tetrahedrite ± sphalerite veins with calcite ± quartz ± barite (sample 4864-B). The distal zone has high Cu (7.8 wt.%), As (1.5 wt.%), Sb (0.96 wt.%), Zn (0.2 wt.%), Ag (155 ppm), and Ba (0.1 wt.%; Table 6). Locally, bornite exhibits supergene alteration to chalcoite (Table 8), malachite, and cuprite.

Away from the network, diorite contains two generations of calcic amphibole (magnesiohornblende and actinolite; Table 7) ± chlorite + calcite + ilmenite + hematite ± apatite with traces of biotite, and irregular albite + chlorite ± bornite microveinlets (sample 4860-C, Fig. 20), whereas siltstone contains calcite ± malachite ± azurite veinlets. A 2 to 10 m-thick barite vein striking 010° and dipping 85°E contains malachite, azurite, and siderite. The vein is partially exposed for 400 m, approximately 300 m southeast of the Las Choicas network (Atalaya mine, Fig. 16b; sample 4863, Fig. 20).

Within the las Choicas-type mineralization, a barite sub-type is represented by well defined vein structures with high Cu (up to 14 wt.%) and Ag (up to 500 g/t). The Choiquitas and Cobrecito mines consist of azurite

± barite ± siderite, and chalcocite ± chalcopyrite ± galena veins with calcite ± barite ± quartz gangue, hosted in sandstone and limestone of the La Manga Formation. The Coloso barite ± siderite ± chalcopyrite vein is hosted in limestone of La Manga Formation (Fig. 16b; Cominor Ingenieros y Proyectos S.A., 1999).

Discussion

Fe Skarns

The main features of the Hierro Indio and Vegas Peladas Fe skarns are: (1) they are both associated with diorite calc-alkaline igneous rocks of the Miocene volcano-plutonic arc emplaced in a continental margin; more differentiated plutons generated skarns with little or no Fe mineralization; (2) diorite margins have been replaced by a thin endoskarn envelope or veins that have epidote-amphibole-magnetite as a common calc-silicate assemblage; (3) in the contact with endoskarns the calcareous protoliths are replaced by zoned garnet ± magnetite exoskarns with minor to trace amounts of pyroxene; (4) garnet compositional ranges are $Grs_{0-66} Adr_{32.5-100}$, and become iron-rich towards crystal rims and towards intermediate exoskarn zones; (5) magnetite and hematite have low MnO (≤ 0.22 wt.%) concentrations; (6) fine-grained magnetite is an early mineral and occurs in equilibrium with diopside-apatite or epidote-amphibole-quartz in endoskarn and with garnet and pyroxene in exoskarn; (8) the largest magnetite and hematite orebodies are accompanied by Fe-rich retrograde assemblages replacing early exoskarn zones; (9) hematite occurs in distal skarn zones associated with retrograde assemblages; and (10) pyrite occurs in minor to trace amounts throughout the skarn system, and is a late mineral in the paragenesis.

The fluid composition and redox conditions prevailing during skarn evolution can be estimated from their mineralogy. Garnet is the most abundant anhydrous calc-silicate mineral at Vegas Peladas and Hierro Indio deposits, and its composition (grossular-andradite series) becomes more iron-rich from core to rim in individual grains and from inner to outer zones at the deposit scale. The presence of massive bodies of magnetite in proximal exoskarn zones, and hypogene hematite in distal zones in association with hydrous calc-silicates such as epidote, actinolite, and ferropargasite, indicates a relatively oxidized environment, with Fe-enrichment with time and declining temperature. Pyroxene is not widespread in the Mendoza Fe skarns, whereas in the Vegas Peladas skarn, it replaces clastic-rich layers and shows a wide compositional range (Hd_{40-74}, Jo_{2-9}). This pyroxene is in equilibrium with andradite-rich garnet in the intermediate zone, suggesting high temperatures of

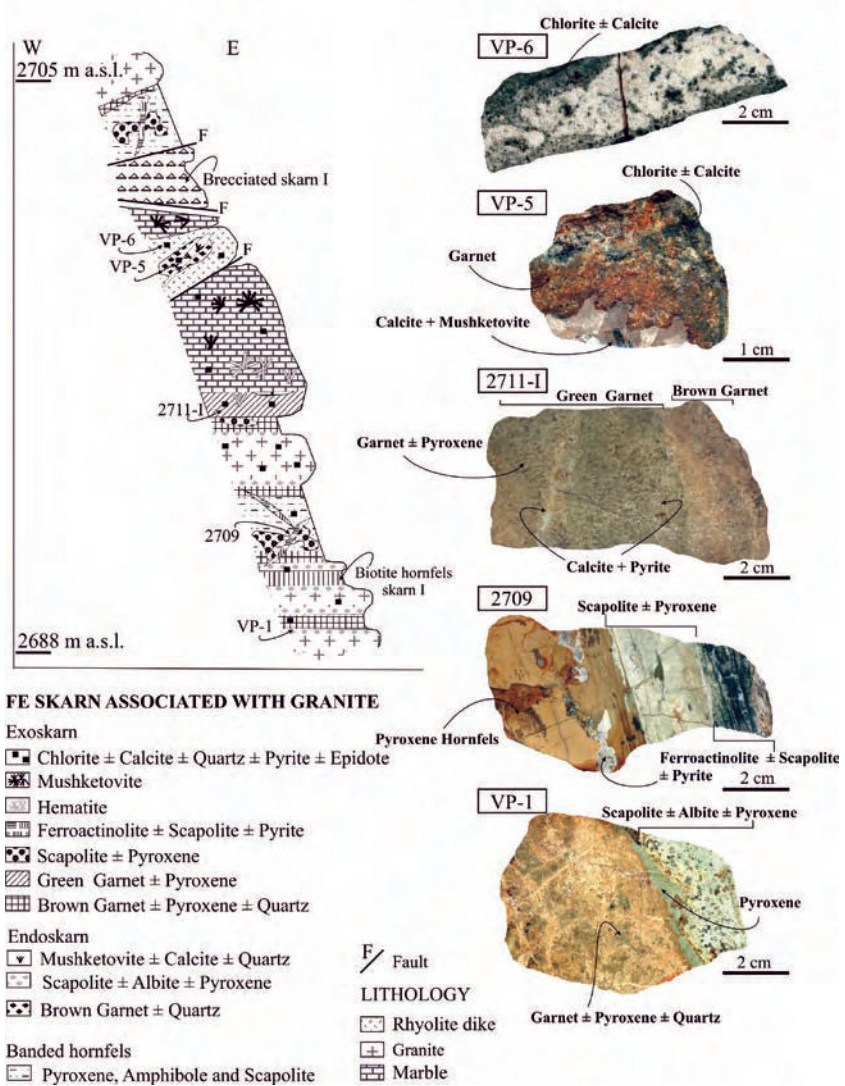


Fig. 15. Schematic E-W profile of the Fe skarn associated with granite and rhyolite, including photographs of the main alteration and mineralization styles in the profile. Sample VP6: chlorite ± calcite alteration of a rhyolite dike. Sample VP5: brown garnet ± quartz endoskarn partially altered to chlorite ± calcite with calcite ± mushketovite-rich pockets. Sample 2711-I: contact between proximal brown garnet ± pyroxene and distal green garnet ± pyroxene exoskarn zones cut by late calcite ± pyrite veinlets. Sample 2709: scapolite ± pyroxene exoskarn in pyroxene hornfels cut by late ferroactinolite ± scapolite ± pyrite vein. Sample VP1: contact between the scapolite ± albite ± pyroxene endoskarn in rhyolite and the brown garnet ± pyroxene ± quartz exoskarn with late calcite ± pyrite. A thin pyroxene envelope separates both zones.

formation (cf. Burton and Taylor, 1982). Most minerals are calcium rich (pyroxene, andradite, Ca-amphibole, epidote, calcite, titanite, apatite) suggesting high calcium activity during skarn formation, most likely due to the dissolution of calcic carbonate protoliths. The presence of calcite accompanying early and late retrograde assemblages in both localities is consistent with an increase in $X(CO_2)$ from the prograde to the retrograde stage. The very low sulfide concentrations in both skarn systems suggest very low reduced sulfur fugacity in the hydrothermal systems.

Homogenization temperatures and salinities (530°–660°C; 60–70 wt.% NaCl equiv.) of fluid inclusions in

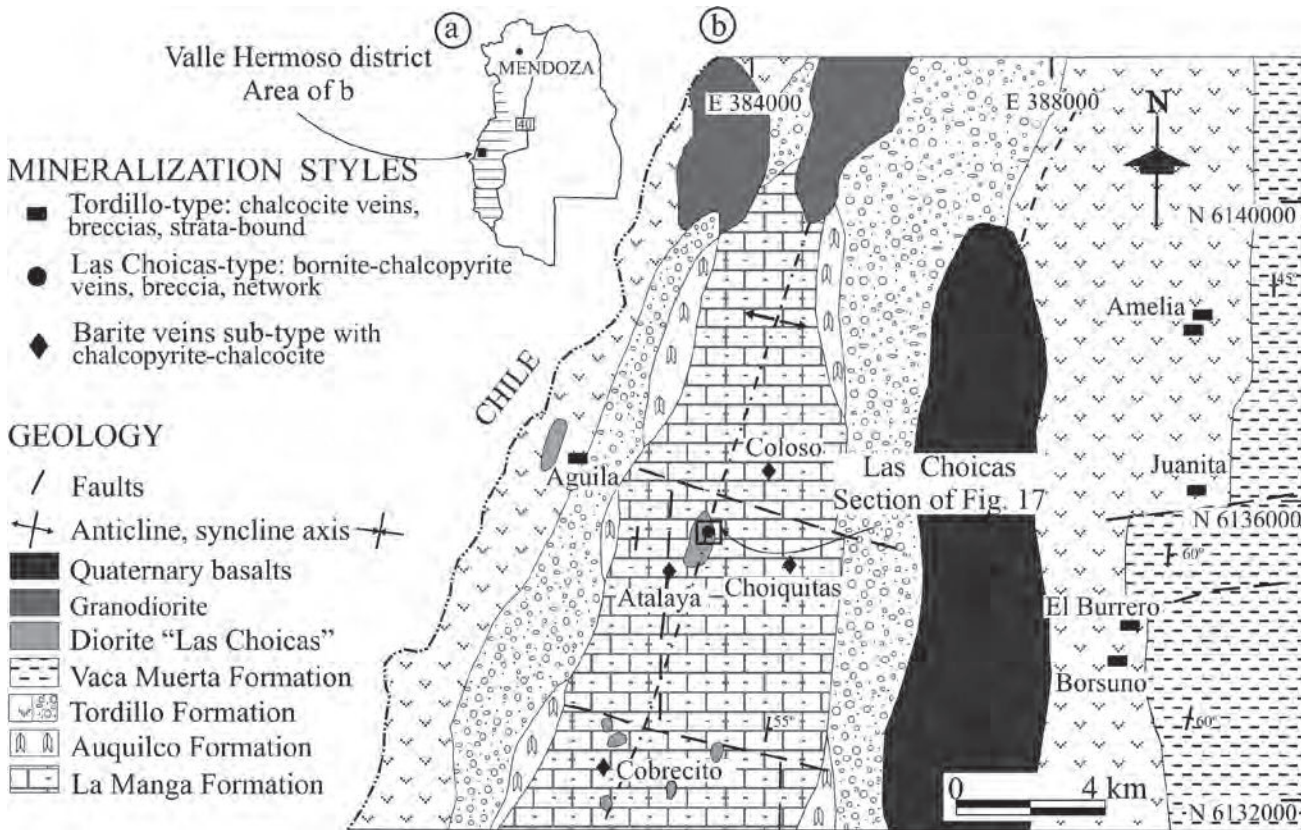


Fig. 16. *a.* Location of Valle Hermoso district in the Thrust Belt of Malargüe. *b.* Geologic map of the Valle Hermoso district showing the location of Las Choicas deposit and other prospects near the mine (modified from Cominor Ingenieros y Proyectos S.A., 1999).

MINERALIZATION

[Dumps icon]	Dumps
[Barite vein, breccia icon]	Barite vein, breccia
[Chalcopyrite ± tetrahedrite icon]	Chalcopyrite ± tetrahedrite
[Bornite ± chalcopyrite icon]	Bornite ± chalcopyrite
[Chalcopyrite icon]	Chalcopyrite
[Pyrite icon]	Pyrite
LITHOLOGY	
[Detritus icon]	Detritus
[Diorite icon]	Diorite
[Siltstone and calcilutite icon]	Siltstone and calcilutite
[Limestone and siltstone icon]	Limestone and siltstone
[Tuffaceous sandstone and siltstone icon]	Tuffaceous sandstone and siltstone

Schematic Cross Section of Las Choicas

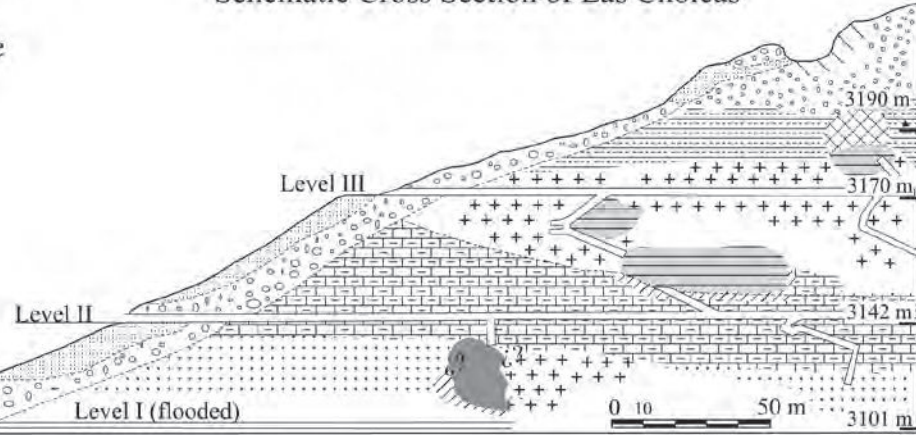


Fig. 17. Schematic cross section of Las Choicas mine showing geology and location of mineralization (modified from Cominor Ingenieros y Proyectos S.A., 1999).

quartz, garnet, and pyroxene in equilibrium with disseminated magnetite from the Vegas Peladas iron skarn, indicate that prograde exoskarn formed from high temperature and high-salinity fluids. Evidence for boiling is absent, suggesting that lithostatic pressures may have prevailed during the early stages of skarn formation. The maximum

hydrostatic pressure of 325 bars determined for the boiling fluids during the retrograde stage corresponds to depths of at least 3.3 km. For non-hydrostatic conditions, 3.3 km of rock with an average density of 2.7 g/cm corresponds to a lithostatic pressure of about 877 bars. At this pressure, high temperatures and salinities allow very high iron solubility

(Hemley and Hunt, 1992; Hemley et al., 1992).

Homogenization temperatures, evidence for boiling, and salinities of fluid inclusions in quartz accompanying massive hematite, epidote, and calcite suggest temperatures in the range of 290° to 436°C, lower pressures (up to 325 bars), and high salinities (32–50 wt.% NaCl equiv.) in fluids responsible for the main stage of iron mineralization. This temperature range correlates with much lower iron solubility in saline fluids (Hemley et al., 1992). This fact, together with gas-phase separation (boiling) may have promoted iron precipitation, although such low pressures (325 bars) generally result in higher metal solubility (Hemley and Hunt, 1992; Hemley et al., 1992). Because magnetite is associated with epidote that replaces garnet, it probably formed at temperatures between the prograde skarn zones (>500°C) and the intermediate hematite + epidote + quartz + calcite zone (<400°C). Thus, the changes of the iron oxide composition in time and space (from magnetite to specular hematite) may be due to temperature decrease, rather than oxygen fugacity increase, as was previously suggested by Ohmoto (2003).

The high-temperature and high-salinity fluids that carried Na, K, Fe, and Cl during early anhydrous skarn formation and preliminary isotopic measurements of early skarn silicates are indicative of a magmatic origin (cf. Kwak and Tan, 1981; Bowman, 1998; Meinert et al., 2005). In addition, high-salinity fluids during the retrograde stage are consistent with a predominance of magmatic rather than meteoric water during iron oxide precipitation.

Cooling and dilution of the hydrothermal system with meteoric water is indicated by low homogenization temperatures (165°–315°C) and salinity (12–14 wt.% NaCl equiv.) in calcite from late, distal quartz + calcite ± chlorite ± titanite ± orthoclase ± pyrite veins in the Vegas Peladas Fe skarn. This general trend to lower temperatures and salinities of hydrothermal fluids with time and away from the diorite stock, the resultant skarn zonation with respect to the diorite stock, and the absence of a separate halite or sylvite source to form high salinity fluids in the region, are indicative of a genetic connection between the hydrothermal fluids and the diorite pluton.

Hierro Indio and Vegas Peladas are similar to calcic iron skarns described by Meinert et al. (2005). The association of iron-rich orebodies with retrograde alteration is typical of many iron skarns (Meinert et al., 2005), indicating that cooling is a major factor in iron precipitation. In addition to these two districts, there are more than 20 recorded skarn occurrences, all of them located along the western

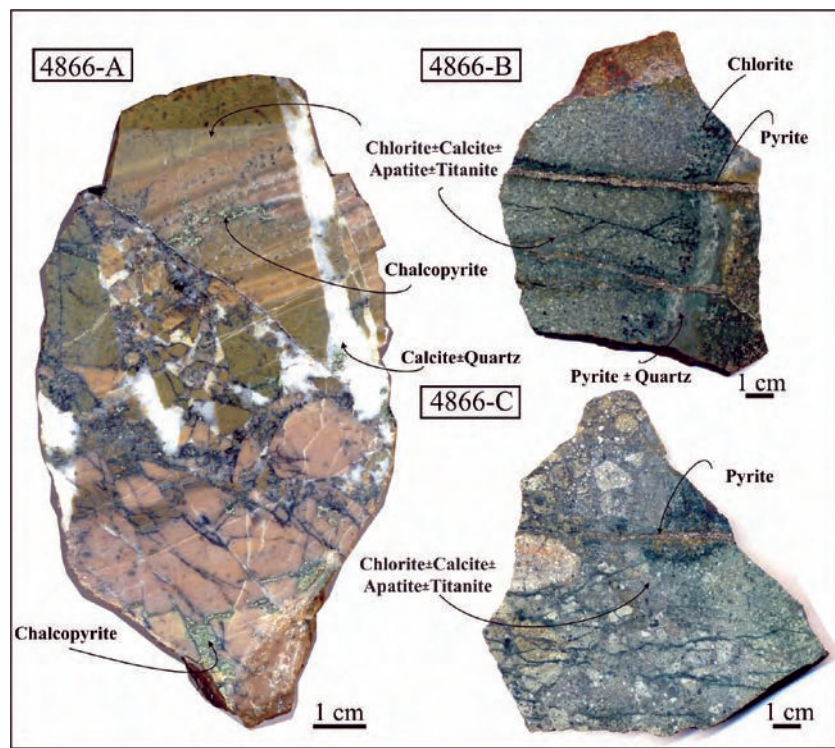


Fig. 18. Photographs of different alteration styles in siltstone, tuffaceous sandstone, and conglomerate in the 3142 m elevation adit. Sample 4866-A: monolithologic breccia of altered siltstone fragments with calcite ± chalcopyrite ± quartz cement. Samples 4866-B and C: tuffaceous conglomerate and sandstone replaced by chlorite + calcite ± apatite ± titanite, and late pyrite ± quartz ± calcite veins with chlorite envelopes.

margin of southwest Mendoza province (Fig. 1, Table 1). Historically, the majority of these skarns have been found in small outcrops with poor exposures, and in several cases steep, rugged terrain covered by modern sediments. Short field seasons and limited access have precluded previous exploration. Thus, these deposits were poorly known and their relation to fundamental geologic processes is just beginning to be understood.

In contrast to previous suggestions that these deposits are Paleogene (Zanettini and Carotti, 1993, and references therein), recent investigations (Nullo et al., 2002) and this contribution demonstrate that iron skarns are associated with diorite (andesite) plutons of the voluminous and widespread upper Miocene magmatism (Huincán Formation). Thus, diorite plutons and andesite dikes and sills have ore potential in numerous, still poorly explored, iron districts throughout the southwest Cordillera Principal of Mendoza province.

Emplacement of these igneous bodies seems to be structurally controlled, for example by anticline and syncline cores. The igneous rocks are typical arc plutons, formed from primitive, mantle-derived magmas with little or no crustal contamination. As with most Fe skarns, they contain more MgO, less K₂O, and less SiO₂ than plutons typically associated with Cu or Zn skarns. Other trace element concentrations, such as Sc and V, and low Rb/Sr ratios are also similar to typical Fe skarn plutons. They have abundant amphibole, strong magnetic response, and they do not

Table 6. Geochemistry of Altered Diorite, Sandstone, Siltstone, and Limestone in the Las Choicas Prospect

Sample	Lower Level		Intermediate Level									Upper Level					
	Host rock	Breccia siltst.	4866-A	4866-B	4865-A	4865-B	4865-C	4865-D	4865-F	4865-E	4865-G	4865-H	4865-I	4860-A	4860-B	4864	4863
			Altered diorite	Altered diorite	Altered diorite	Altered diorite	Altered diorite	Altered diorite	Altered diorite	Altered siltst.	Altered limest.	Pyrite zone	Altered limest.	Network diorite	Network siltst.	Network siltst.	Barite breccia
(wt.%)																	
Fe	3.67	>10.00	4.51	6.61	6.56	4.87	6.26	4.92	2.66	>10.00	1.84	5.97	2.02	4.17	7.65		
Mn	0.08	0.10	0.05	0.17	0.13	0.07	0.08	0.03	0.04	0.05	0.14	0.06	0.03	0.03	0.01		
Mg	1.19	1.83	2.75	2.90	2.66	1.94	0.83	1.35	0.30	0.03	0.53	1.83	1.21	0.01	0.01		
Ca	10.49	4.32	3.15	4.95	3.92	4.24	8.60	6.69	25.18	0.10	29.54	0.63	11.24	0.17	0.04		
Cu	1.74	0.08	10.10	4.35	5.92	6.26	0.05	11.97	14.21	0.16	1.81	10.39	4.30	7.85	0.18		
S	1.67	8.67	4.02	1.91	3.27	2.53	3.63	5.09	5.71	>10.00	0.93	2.48	0.91	3.01	0.22		
(ppm)																	
V	139	158	68	77	69	66	107	87	18	32	45	71	74	13	6		
Ni	15	23	4019	3791	3393	2901	114	263	418	56	23	276	43	<1	2		
Zn	219	21	96	38	47	106	119	23	441	92	63	34	20	2121	164		
Ga	7	8	9	10	9	10	15	8	<2	<2	3	11	6	<2	<2		
As	<5	6	94	6	13	20	6	61	538	95	6	<5	<5	15 270	851		
Sb	6	<5	13	9	<5	<5	<5	<5	<5	11	<5	9	<5	9655	961		
Sr	29	40	30	41	52	30	26	31	81	3	282	12	112	54	1838		
Y	12	11	10	10	9	11	22	11	4	3	7	10	12	3	<1		
Zr	2	15	2	4	9	38	65	6	<1	2	15	32	41	<1	<1		
Mo	<1	4	7	11	11	5	5	79	8	18	7	3	1	9	21		
Ba	11	43	66	48	67	26	21	14	5	19	241	113	10	1216	>2000		
Ag	4	<0.5	16	8	8	9	<0.5	25	48	3	3	324	114	155	5		
Co	7	166	35	109	86	30	39	44	41	355	9	23	4	3	<1		
Cr	16	5	275	219	153	179	19	12	2	2	7	85	17	3	<1		
Hg	<2	<2	<2	<2	<2	<2	<2	<2	<2	<2	<2	<2	<2	41	<2		
Li	12	23	24	38	31	21	9	15	2	<1	7	25	10	<1	<1		
U	41	29	10	22	21	<10	32	25	92	<10	133	<10	47	<10	<10		
Bi	<5	<5	<5	<5	<5	<5	<5	<5	<5	<5	<5	18	<5	<5	<5		
Cd	<1	<1	<1	<1	<1	<1	<1	<1	1	<1	<1	<1	<1	16	<1		
Pb	<2	7	15	6	11	3	11	9	79	199	13	3	3	17	71		
Sc	8	10	7	9	10	7	10	8	<5	<5	<5	8	12	<5	<5		
La	20	25	8	8	6	11	24	15	13	9	13	6	9	3	<1		
Ce	27	30	11	8	6	8	33	21	13	19	13	<5	12	<5	<5		

*Notes*¹ Diorite-siltstone contact.

Altered and mineralized protoliths from las Choicas prospect were analyzed by ICP and Au by fire assay at Alex Stewart (Assayers) Argentina S.A. Nb (<1 ppm), Sn (<20 ppm), Ta (<10 ppm), W (<20 ppm), Au (<0.01 ppm), Te (<10 ppm), Th (<10 ppm), Tl (<5 ppm), Se (<10 ppm) below detection.

contain quartz or primary ilmenite. The magmatic magnetite contains high TiO₂ (up to 10 wt.%), compared to hydrothermal magnetite (up to 4 wt.% in diorite and 0.1 wt.% in skarn; Fig. 7b). Widespread, early hydrothermal alteration of diorite associated with iron skarns and its mineralogical zonation towards sedimentary protolith contacts described in this contribution, can be used as an exploration guide, particularly in areas of poor exposure.

Las Choicas Cu-(Ag) Prospect

The alteration and mineralization at Las Choicas occurs at the contact of the La Manga Formation with a diorite pluton. This diorite has a significant positive Eu anomaly and its N-MORB-normalized trace element patterns show positive Ta and Nb anomalies with respect to Th and Ce, and have high Ti, features uncommon in the Miocene diorite associated with Fe skarns and of magmas derived from sub-arc mantle sources (Kay and Mpodozis, 2002). Except

for traces of garnet in the altered diorite and a thin prehnite envelope locally replacing a carbonate-rich layer at the contact with altered diorite, calc-silicate minerals typical of Cu skarns have not been found at Las Choicas. The dominant early chlorite + calcite ± albite ± scapolite ± apatite ± ilmenite alteration that introduced Fe-Na-Ca-Mg-Ti-P to the igneous and sedimentary protoliths, and late stage calcite + albite ± quartz accompanying copper sulfides in igneous and sedimentary rocks with Ni, Cr, and Co anomalies, are features not common in Cu skarn deposits. Also absent are potassic and sericite alteration zones and widespread copper sulfide-quartz vein stockwork typical of porphyry Cu deposits. Widespread ilmenite and apatite, the relatively high copper concentrations, intense sodium-calcium metasomatism associated with copper sulfides, and the presence of millerite at Las Choicas are uncommon in porphyry copper deposits.

The alteration and mineralization at Las Choicas have



Fig. 19. Photographs of different alteration styles in diorite, siltstone, and limestone in the 3170 m elevation adit. Sample 4865-A: Altered diorite with a swarm of parallel fractures resembling sheeted veins, filled with calcite \pm quartz \pm bornite \pm chalcopyrite and a green chlorite alteration envelope; these veinlets connect bornite clots. Samples 4865-B and -C: Intensely altered diorite with more than one generation of very thin sinuous calcite veinlets that connect disseminated bornite \pm chalcopyrite grains, and thin bornite \pm chalcopyrite veinlets with calcite \pm albite \pm quartz envelopes. Sample 4865-D: Early thicker veins with parallel walls, lenticular veins with calcite \pm bornite \pm chalcopyrite infill, and a colorless albite alteration envelope are cut and offset by bornite \pm chalcopyrite, albite, and calcite veinlets. Sample 4865-F: Thin prehnite envelope at the contact between altered diorite and siltstone. Sample 4865-E: Calcite \pm bornite \pm chalcopyrite \pm albite \pm quartz alteration has invaded early calcite \pm chlorite \pm titanite \pm apatite alteration of siltstone along laminations (thick veins) and fractures (thin veinlets). Sample 4865-F: Late stage of calcite \pm bornite \pm chalcopyrite \pm albite \pm quartz veins. Sample 4865-G: Outer pyrite-rich zone with Co anomalies. Sample 4865-I: Alteration zone with prehnite and calcite \pm chlorite \pm rutile \pm apatite and bornite \pm chalcopyrite passes gradually to a fresh laminated limestone with clastic intercalations cut by late calcite veins.

Table 7. Representative Electron Microprobe Analyses of Hydrothermal Amphibole, Albite, Chlorite, Prehnite, and Apatite from the Altered Diorite and Limestone in the Las Choicas District

Sample:	4860-C-1	4865-D-1	4860-C-2	Sample:	4865-D-2	4865-D-3	Sample:	4865-D-4	4865-D-5	Sample:	4865-F-1	4865-F-2	4865-F-3	Sample:	4860-C-3
Mineral															
(wt.%)	Mg-hornblende ²	Actinolite ²	Albite	(wt.%)	Silica	(wt.%)	Magnesian chamosite ³	(wt.%)	Prehnite	(wt.%)	SiO ₂	TiO ₂	Al ₂ O ₃	SiO ₂	Apatite
SiO ₂	51.53	51.34	50.09	SiO ₂	67.29	66.94	SiO ₂	30.22	31.41	SiO ₂	n.d.	n.d.	n.d.	SiO ₂	n.d.
TiO ₂	1.04	0.29	1.25	TiO ₂	n.d.	n.d.	TiO ₂	0.18	0.03	TiO ₂	n.d.	n.d.	n.d.	TiO ₂	n.d.
Al ₂ O ₃	4.16	3.46	4.40	Al ₂ O ₃	19.77	19.91	Al ₂ O ₃	14.31	15.03	Al ₂ O ₃	24.15	24.21	23.64	Al ₂ O ₃	n.d.
FeO	15.49	10.95	14.97	FeO	n.d.	n.d.	FeO	19.80	18.91	FeO	n.d.	n.d.	n.d.	FeO	n.d.
MnO	n.d.	n.d.	MnO	n.d.	n.d.	MnO	n.d.	n.d.	MnO	n.d.	n.d.	n.d.	MnO	n.d.	
MgO	13.86	16.63	14.01	MgO	n.d.	n.d.	MgO	18.19	17.99	MgO	n.d.	n.d.	n.d.	MgO	n.d.
CaO	10.84	9.65	11.08	CaO	0.63	0.77	CaO	0.26	0.12	CaO	28.05	27.79	27.81	CaO	52.55
Na ₂ O	1.39	0.75	1.51	Na ₂ O	11.74	11.65	Na ₂ O	n.d.	0.01	Na ₂ O	0.01	0.02	0.01	Na ₂ O	n.d.
K ₂ O	0.36	0.16	0.40	K ₂ O	0.06	0.12	K ₂ O	0.01	0.02	K ₂ O	n.d.	n.d.	n.d.	K ₂ O	n.d.
P ₂ O ₅	—	—	P ₂ O ₅	—	—	P ₂ O ₅	—	—	P ₂ O ₅	—	—	—	P ₂ O ₅	39.65	
F	—	—	F	—	—	F	—	—	F	—	—	—	F	2.41	
Cl	—	—	Cl	—	—	Cl	—	—	Cl	—	—	—	Cl	0.76	
Total	98.67	93.24	97.70	Total	99.5	99.40	Total	82.96	83.52	Total	95.92	95.59	95.38	Total	95.37
(Cations based on 23 oxygens)															
Si	7.46	7.65	7.35	Si	11.85	11.82	Si	6.51	6.65	Si	6.00	6.00	6.06	Si	0.00
Al _{IV}	0.54	0.35	0.65	Al	4.11	4.14	Al _{IV}	1.49	1.35	Al	3.91	3.93	3.85	Al	0.00
Al _{VI}	0.17	0.26	0.11	Ti	0.00	0.00	Al _{VI}	2.14	2.40	Ti	0.00	0.00	0.00	P	13.81
Ti	0.11	0.03	0.14	Fe	0.00	0.00	Ti	0.03	0.00	Fe	0.00	0.00	0.00	Ti	0.00
Fe ²⁺	1.88	1.37	3.06	Mg	0.00	0.00	Fe	3.57	3.35	Mg	0.00	0.00	0.00	Fe	0.00
Mg	2.99	3.69	1.84	Ca	0.12	0.15	Mg	5.84	5.68	Ca	4.13	4.10	4.11	Mg	0.00
Ca	1.68	1.54	1.74	Na	4.01	3.99	Ca	0.06	0.03	Na	0.00	0.00	0.00	Ca	23.17
Na	0.39	0.22	0.43	K	0.01	0.03	Na	0.00	0.00	K	0.00	0.00	0.00	Na	0.00
K	0.07	0.03	0.07	Orthoclase	0.30	0.63	K	0.00	0.00	—	—	—	—	K	0.00
				Albite	96.81	95.88								F	3.14
Mg/(Mg+Fe ²⁺)	0.61	0.73	0.63	Anorthite	2.89	3.49	Fe ²⁺ /(Fe ²⁺ +Mg)	0.76	0.74					Cl	0.53

*Notes*¹All iron as FeO.²Structural formulas were calculated after Leake et al. (1997).³Structural formulas were calculated after Newman and Brown (1987).

Chlorite classification after Bailey (1980) and McLeod and Stanton (1984).

— = not analyzed; n.d. = not detected.

features in common with IOCG deposits located in the Central Andes Cordillera of Perú and Chile (Sillitoe, 2003; Williams et al., 2005), including: (1) spatial and genetic relationship to mafic diorite intrusions and associated cogenetic dikes; (2) ore controls consisting of brittle fracture systems that affected all rock types, and breccias; (3) widespread chlorite + albite + apatite alteration of host rocks; amphibole, epidote, and traces of biotite have also been observed in diorite and sandstone; (4) Sb, As, Co, Ni, with Mo and Zn anomalies; (5) copper mineralization is associated with calcic-sodic alteration, similar to several examples of Central Andes IOCG deposits (Raúl Condestable, El Espino); (6) although present, quartz occurs only in minor to trace amounts accompanying copper mineralization and a distal pyrite-rich zone; (7) numerous calcite veins constitute the uppermost manifestation of the deposit. However, potassic alteration described for numerous deposits and iron ore in the form of magnetite and hematite are not found at Las Choicas, although altered diorite contains relict biotite crystals, and in the periphery of the network where amphibole is dominant, hematite and ilmenite occur, but the spatial distribution of these hydrothermal minerals is not well constrained.

Numerous examples of IOCG deposits of southern Perú and northern Chile, like Candelaria-Punta del Cobre (Marschik and Fontboté, 2001; Williams et al., 2005) are zoned, with a magnetite-actinolite-apatite deeper zone that grades upwards to a hematite-chlorite-sericite-rich zone. Thus, in a partially explored system like Las Choicas, it is possible that the iron oxide-rich deeper zones have not yet been reached. Instead of hematite or magnetite, ilmenite is a widespread, early hydrothermal mineral in the investigated diorite outcrops. This oxide has been described as an ancillary mineral in several prospects of southern Perú (Injoque, 2002).

Other characteristics of Las Choicas alteration and mineralization are similar to manto-type (stratabound) Cu deposits of northern and central Chile, such as the abundance of carbonates in all stages of the alteration and mineralization, chloritization and albitization of wall rocks, the presence of Ag anomalies and a marked deficiency in gold, and the concentrically zoned sulfide assemblage, with a bornite-chalcopyrite core, grading outwards to chalcopyrite, chalcopyrite (tetrahedrite), and a pyrite halo (Espinoza, 1994; Espinoza et al., 1996; Sillitoe, 2003). Nevertheless, somewhat similar zoning (without tetrahedrite) is described for the vein-like Mina Panulcillo (Hopper and Correa, 2000) and, with chalcocite in the core in addition to bornite, in the Mina Justa IOCG deposits (Moody et al., 2003).

Manto-type Cu deposits in Chile are hosted in volcanic and volcanioclastic rocks of the Jurassic-Lower Cretaceous volcanic arc and intra-arc basin (Dallmeyer et al., 1996; Maksaev and Zentilli, 2002) near hypabyssal intrusive rocks with ages 20 to 30 m.y. younger than the host volcan-

Table 8. Representative Compositions of Bornite, Chalcopyrite, Chalcocite, and Millerite

Sample	4860-C-1	4860-C-2	4865-C-1	4865-C-2	4860-C-3	4860-C-4	4865-C-3	4865-C-4
	Bornite		Chalcopyrite		Chalcocite		Millerite	
(wt %)								
S	26.24	25.89	34.74	32.67	22.52	22.86	33.28	34.03
Cu	64.81	63.75	34.68	42.92	77.70	77.23	0.39	0.00
Fe	10.51	9.70	29.31	22.71	0.16	0.20	1.07	0.38
Ni	0.10	0.07	0.01	0.00	0.00	0.03	62.68	64.63
Co	0.00	0.01	0.03	0.00	0.07	0.00	0.86	0.86
Total	101.66	99.42	98.77	98.30	100.45	100.32	98.28	99.90

ic rocks (Espinoza et al., 1996). Most of these hypabyssal bodies are barren and do not exhibit hydrothermal alteration. Iron oxide in the form of specularite is also present in the uppermost levels of these deposits (Mantos Blancos, Buena Esperanza; Espinoza et al., 1996). This geological setting—not present at Las Choicas—is somewhat similar to the Tordillo-type Cu prospects located 1200 m NW and 6 km E of Las Choicas (Fig. 16b). These prospects are hosted in andesitic lava flows and volcanic autobreccias intercalated in sandstone and conglomerate, or at the contact between andesite flows and sills in the upper portions of The Tordillo Formation, capped by marine sedimentary rocks of the Vaca Muerta Formation. The Aguila mine is the only example of this type located close to a small diorite outcrop (Fig. 16b). All these strata were affected by faults that may have played an important role in channeling of hydrothermal fluids (Cominor Ingenieros y Proyectos S.A., 1999). Mineralization consists of chalcocite, minor chalcopyrite, and bornite with secondary chalcocite, malachite, azurite, and cuprite as irregular veins and veinlets, vesicle fillings, and forming the matrix of the breccia. Volcanic rocks show chloritization and serpentinization of mafic minerals and ground mass, sericite and carbonate alteration of feldspars, and prehnite and calcite filling vesicles and open spaces (Cominor Ingenieros y Proyectos S.A., 1999). Samples contain up to 8% Cu, 25.2 g/t Ag, and 0.12 g/t Au (Cominor Ingenieros y Proyectos S.A., 1999).

Williams (1999) and Pollard (2000) classified some manto-type deposits as members of the IOCG clan. Other authors consider manto-type deposits as shallow manifestations of the IOCG type (Vivallo and Enriquez, 1998; Vivallo, 2005). The Las Choicas- and Tordillo-type deposits share some of the characteristics of these systems, but at present, it is not possible to classify them precisely.

Conclusions

In the Andes Cordillera of southwestern Mendoza province, a north-south (34° – 36° S) trending iron skarn belt occurs in association with mantle-derived diorites of the upper Miocene plutonic arc. These skarns are similar to worldwide Fe calcic skarns associated with primitive plutons and formed from high-temperature, high-salinity fluids with a strong magmatic signature. Cooling was probably the main mechanism for Fe oxide precipitation and

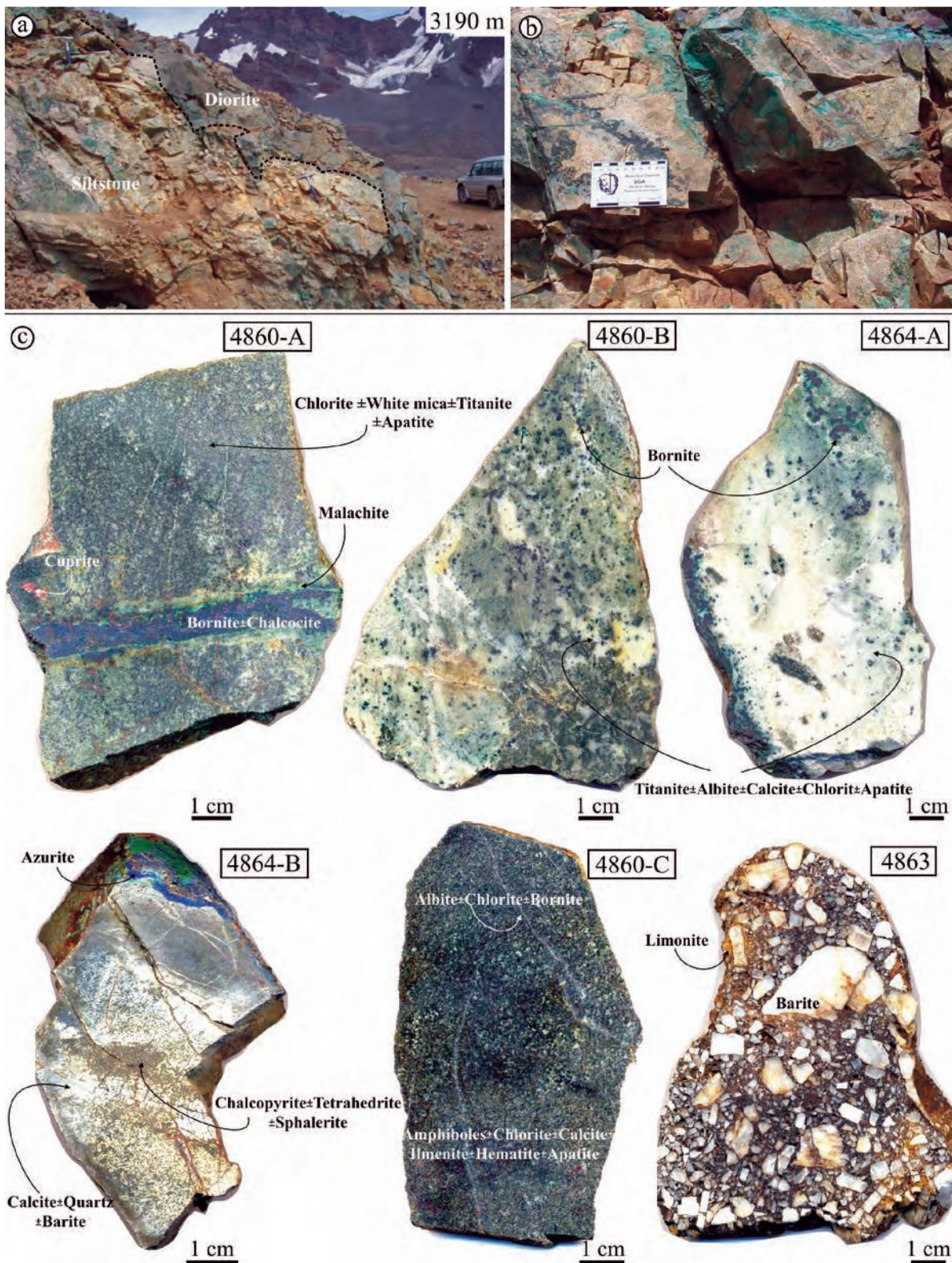


Fig. 20. **a, b.** Photographs looking west of stockwork at 3190 m elevation, at the contact of diorite with siltstone. **c.** Photographs of samples. Sample 4860-A: bornite vein cuts altered diorite; bornite exhibits supergene alteration to chalcocite, malachite, and cuprite. Sample 4860-B: contact zone (altered diorite-siltstone) with disseminated bornite ± chalcopyrite. Sample 4864-A: titanite ± albite ± calcite ± chlorite ± apatite alteration of siltstone accompanying bornite. Sample 4864-B: distal chalcopyrite ± tetrahedrite ± sphalerite veins and veinlets with calcite ± quartz ± barite envelopes. Sample 4860-C: alteration in distal diorite walls of the network. Sample 4863: brecciated barite ± siderite (now converted to limonite) vein, Atalaya mine.

concentration in the orebodies. District variations in the skarn and ore mineralogy may reflect local differences in host-rock composition and/or fluid evolution.

West of the Fe skarn belt, there are several Cu-(Ag) prospects that have been grouped as Las Choicas type- and Tordillo type-Cu deposits. The Las Choicas deposit shares several features characteristic of IOCG deposits of Perú and Chile, and also of the manto-type Cu deposits of northern and central Chile. Thus, this deposit may represent either the continuation of the IOCG belt located in the Coastal Cordillera of southern Perú and northern Chile (13° – $33^{\circ}30' S$) that ends at the La Africana Cu-prospect in Chile at the latitude of Santiago (Sillitoe, 2003), or the continuation of the Chilean manto-type belt. If this is the case, Las Choicas and the other Cu prospects would represent the first reported occurrence of IOCG-type and manto-type deposits in this segment of the Andes Cordillera of Argentina, and implies that geologic conditions that favor the development of these deposits may be more widespread than previously thought. The key alteration and mineralization characteristics of the Las Choicas deposit described in this investigation can be used in exploration of other Cu prospects in the Valle Hemoso district, in poorly known Cu and Cu-Fe prospects like Arroyo Nieves Negras, Arroyo Overas, Laguna Diamante, and Arroyo La Línea, and in areas with Cu boulder detritus near the Chilean border (Fig. 1).

Acknowledgments

This work forms part of a project financed by CONICET (PIP N° 2726) and a Student Research Grant awarded by SEG (Society of Economic Geologists). We express our appreciation to G. Mas and L. Bengochea (CONICET-U. N. del Sur, Bahía Blanca) for their collaboration in the fluid inclusion study of the Vegas Peladas Fe skarn, Colombo Tassinari (CPGeo- Geosciences Institute, San Pablo University, Brazil) and S. O’Leary (CONICET- U. N. del Comahue) for their collaboration in obtaining isotopic ages, A.M. Izard (Geology Department at the Oviedo University, Spain), R. Etcheverry, and K. Mykietiuk (INREMI, U. N.de La Plata) for their collaboration in microprobe analyses, A. Impiccini (CIMAR, U.N. del Comahue) for X-ray analyses, G. Ré Kuhl (Alto Américas), and G. Páez, and M.G. Guillot (CONICET, INREMI) for their help in the field work. We thank G. Mark and M. Cruse for their helpful and constructive reviews, which led to an improvement of the manuscript. Finally, we wish to thank D. Lentz and J. Richards for their careful examination of the manuscript and for their overall dedication as the Guest Editor and Editor.

References

- Angelelli, V., 1950, Recursos Minerales de la República Argentina. I. Yacimientos Metalíferos: Revista Serie Ciencias Geológicas, Instituto Nacional de Investigación de las Ciencias Naturales, Museo Argentino de las Ciencias Naturales “Bernardino Rivadavia”, Buenos Aires, 543 p.
- Angelelli, V., 1984, Yacimientos metalíferos de la República Argentina: Comisión de Investigaciones Científicas de la provincia de Buenos Aires (CICBA), La Plata, v. 1, 391 p.
- Angelelli, V., Fernandez Lima, J.C., Herrera, A., and Aristarain, L., 1970, Descripción del Mapa Metalogenético de la República Argentina, Minerales Metalíferos: Dirección Nacional de Geología y Minería, Buenos Aires, Anales 15, p. 7–172.
- Arrospide, A., 1972, Depósitos de minerales de hierro de Vegas Peladas Mina “Nenche”, dpto. de Malargüe, Mendoza, República Argentina: Revista de la Asociación Argentina de Mineralogía, Petrología y Sedimentología, v. 3, p. 117–131.
- Bailey, S.W., 1980, Summary and recommendations of AIPEA Nomenclature Committee: Clays and Clay Minerals, v. 28, p. 73–78.
- Baldauf, p.G., Stephens, G.M., Kunk, M., and Nullo, F., 1992, Argon-Argon ages for the Huincán intrusive suite and their implications for the structural development of the Andean foreland, Southern Mendoza province, Argentina [abs.]: Geological Society of America, Boulder, Abstract with Programs 24, p. A188.
- Barriónuevo, L.A., 1953, Sobre los yacimientos cupríferos de los cerros la Virgen y Mirano, provincia de Mendoza: Informe Geológico-Minero Dirección General Fabricaciones Militares: Biblioteca del Servicio Geológico Minero Argentino, Buenos Aires, 31 p. and appendixes (6).
- Barriónuevo, L.A., and Elizalde, C.O., 1950, Información preliminar sobre algunos yacimientos de la provincia de Mendoza (hierro, cobre y molibdeno): Dirección General de Fabricaciones Militares: Biblioteca del Servicio Geológico Minero Argentino, Buenos Aires, 88 p., 12 appendixes and maps
- Bellieni, G., Visentin E.J., and Zanettin B., 1996, Use of chemical TAS diagram (Total Alkali Silica) for classification of plutonic rocks: Problems and suggestions: I.U.G.S.: Subcommission on the Systematics of Igneous Rocks, Contribution N° 157, 35 p.
- Bodnar, R.J., Burnham, C.W., and Sterner, S.M., 1985, Synthetic fluid inclusions in natural quartz, III: Determination of phase equilibrium properties in the system H_2O -NaCl to $1000^{\circ}C$ and 1500 bars: Geochimica et Cosmochimica Acta, v. 49, p. 1861–1873.
- Bonfils, V.H., 1972, Información preliminar sobre los afloramientos 3 y 4 de la mina Hierro Indio, Dirección General de Minería: Biblioteca del Servicio Geológico Minero Argentino, Buenos Aires, 27 p. and appendixes.
- Bouza, p., 1991, Descripción Geológica y caracterización petrográfica de las vulcanitas cenozoicas aflorantes entre los arroyos Montañas y El Yeso, Cordillera Principal, Mendoza: Unpublished Bachelors dissertation, Facultad de Ciencias Exactas y Naturales, Universidad de Buenos Aires, 112 p.
- Bowman, J.R., 1998, Stable-isotope systematics of skarns, in Lentz D., ed., Mineralized intrusion-related skarn systems: Mineralogical Association of Canada, Short

- Course Series, v. 26, p. 99–145.
- Boynton, N.V., 1989, Cosmochemistry of the rare earth elements: Condensation and evaporation processes, in Lipin, B.R., and McKay, G.A., eds., Geochemistry and mineralogy of rare earth elements: Reviews in Mineralogy 21, Mineralogical Society of America, p. 1–24.
- Burton, J., and Taylor, L., 1982, The f_{O_2} and f_{S_2-T} stability relations of Hedenbergite and of Hedenbergite-Johannsenite solid solutions: Economic Geology, v. 77, p. 764–783.
- Centeno, R., and Fallet, J., 1999, Yacimieno de Cobre Las Choicas, Mendoza, in Zappettini, E. ed., Recursos Minerales de la República Argentina: Instituto de Geología y Recursos Minerales, Servicio Geológico Minero Argentino, SEGEMAR, Anales 35, p. 1553–1555.
- Cominor Ingenieros y Proyectos S.A., 1999, Consideraciones Geológico-Económicas de las manifestaciones minerales del distrito cuprífero Valle Hermoso, provincia de Mendoza, Argentina, 27 p. and 5 appendixes (93 p. and 3 maps).
- Dallmeyer, R., Brown, M., Grocott, J., Taylor, G., Treloar, P., 1996, Mesozoic magmatic and tectonic events within the Andean plate boundary zone, 26°–27°30'S, north Chile: Constraints from $^{40}\text{Ar}/^{39}\text{Ar}$ mineral ages: Journal of Geology, v. 104, p. 19–40.
- Davidson, J.P., Fergusson, K.M., Colucci, M.T., and Dungan, M.A., 1988, The origin and evolution of magmas from the San Pedro-Pellado volcanic complex, south Chile: Multicomponent sources and open system evolution: Contributions to Mineralogy and Petrology, v. 100, p. 429–445.
- Dawson, K., Franchini, M., Cravero, O., Zanettini, J.C., and Márquez, M., 2000, Skarn deposits in Argentina: Studies in La Rioja, San Juan, Mendoza, Neuquén and Chubut provinces: Recursos Minerales 12, Servicio Geológico Minero Argentino: Biblioteca del Servicio Geológico Minero, Buenos Aires, 165 p.
- Dessanti, R.N., 1973, Descripción Geológica de la Hoja 29-b, Bardas Blancas, Provincia de Mendoza: Servicio Nacional de Geología y Minería, Buenos Aires, Boletín n° 139, 70 p.
- Devito, H.A., 1954, Estudio de los yacimientos de cobre de la denominada región de Valle Hermoso, Distrito minero N° 2, Laguna Blanca, dpto de Malargüe, provincia de Mendoza, Argentina: Biblioteca del Servicio Geológico Minero Argentino, Buenos Aires, 54 p. and appendixes.
- Dirección General Fabricaciones Militares (DGFM), 1969, Informe sobre las Investigaciones Geológico-Mineras realizadas en la Provincia de Mendoza y Resultados Obtenidos, Plan Cordillerano Centro: Biblioteca del Servicio Geológico Minero Argentino, Buenos Aires, 79 p. and 18 appendixes
- Elizalde, C.O., and Gonzalez Laguinge, H., 1954, Informe Geológico-Geofísico del yacimiento de magnetita de Hierro Indio, departamento San Rafael, provincia de Mendoza, Dirección General de Fabricaciones Militares: Biblioteca del Servicio Geológico Minero Argentino, Buenos Aires, 79 p. and appendixes.
- Espinosa, J.I., 1994, Yacimientos de Cu tipo manto como mineralizaciones económicas en sistemas geotermiales mesozoicos andinos, relación al metmorfismo, volcanismo y ambiente geotectónico: 7º Congreso Geológico Chileno, Concepción, Chile, Actas 2, p. 1565–1570.
- Espinosa, S., Véliz, H., Esquivel, J., Arias, J., and Moraga, A., 1996, The Cupriferous Province of the Coastal range, Northern Chile, in Camus, F., Sillitoe, R., and Petersen, R., eds., Andean copper deposits: New discoveries, mineralization, styles, and metallogeny: Society of Economic Geologists, Special Publication Number 5, p. 19–32.
- Fallet, J., 1972, Informe Geológico-Minero del yacimiento de hierro Tito, departamento Malargüe, Mendoza, Dirección General de Minería de Mendoza: Biblioteca del Servicio Geológico Minero Argentino, 7 p. and appendices.
- Franchini, M.B., 2005, World skarn deposits: Skarns of Argentina: Economic Geology 100th Anniversary Volume, p. 299–336.
- Franchini, M., and Dawson, K., 1999, Las Manifestaciones Metálicas asociadas a Skarns del Suroeste de Mendoza y Noroeste de Neuquén: Instituto de Geología y Recursos Minerales, Seervicio Geológico Minero Argentino, SEGEMAR, Anales 35, p. 1535–1545.
- Franchini, M.B., Lopez-Escobar, L., Schalamuk, I.B., and Meinert, L., 2003, Magmatic characteristics of the Paleocene Cerro Nevazón region and other late Cretaceous to early Tertiary calc-alkaline subvolcanic to plutonic units in the Neuquén Andes, Argentina: Journal of South American Earth Sciences, v. 16, p. 399–421.
- Futa, K., and Stern, C.R., 1988, Sr and Nd isotopic and trace element compositions of recent volcanic centers of the Southern Andes: Implications for petrogenesis of orogenic magmas along a continental margin: Earth and Planetary Sciences Letter, v. 88, p. 253–262.
- Gulisano, C.A., and Gutiérrez Pleimling, A.R., 1995, Field Guide: The Jurassic of the Neuquén Basin, Mendoza Province: Asociación Geológica Argentina, serie E, n° 3, 103 p.
- Haller, M., Nullo, F., Proserpio, C.P., Párica, p., Cagnoni, M., and Walker, G., 1985, Major element geochemistry of early Tertiary Andean Volcanic (34°–36°S): Comunicaciones 35, Santiago, Chile, p. 97–100.
- Hemley, J.J., Cygan, G.L., Fein, J.B., Robinson, G.R., and D'Angelo, W.M., 1992, Hydrothermal ore-forming processes in the light of studies in rock-buffered systems— I: Iron-copper-zinc-lead sulfide solubility relations: Economic Geology, v. 87, p. 1–22.
- Hemley, J.J., and Hunt, J.P., 1992, Hydrothermal ore-forming processes in the light of studies in rock-buffered systems— II: Some general geologic applications: Economic Geology, v. 87, p. 23–43.
- Hildreth, W.E., and Moorbat, S., 1988, Crustal contribution to arc magmatism in the Andes of Central Chile: Contribution to Mineralogy and Petrology, v. 98, p. 455–489.
- Hitzman M., Oreskes, N., and Einaudi, M., 1992, Geological characteristics and tectonic setting of Proterozoic iron oxide (Cu-U-Au-REE) deposits: Precambrian Research, v. 58, p. 241–287.
- Hopper, D., and Correa, A., 2000, The Panulcillo and Teresa

- de Colmo copper deposits: Two contrasting examples of Fe-ox-Cu-Au mineralization from the Coastal Cordillera of Chile, in Porter, T.M., ed., Hydrothermal iron oxide copper-gold and related deposits: A global perspective: Adelaide, Australian Mineral Foundation, p. 177–189.
- Injoque, E.J., 2002, Fe oxide-Cu-Au deposits in Perú: An integrated view, in Porter, T.M. ed., Hydrothermal iron oxide copper-gold and related deposits: A global perspective: Adelaide, PGC Publishing, v. 2, p. 97–113.
- Irvine, T., and Baragar, W., 1971, A guide to the chemical classification of the common volcanic rocks: Canadian Journal of Earth Sciences, v. 8 (5), p. 523–548.
- Kay, S., and Mpodozis, C., 2002, Magmatism as a probe to the Neogene shallowing of the Nazca plate beneath the modern Chilean flat-slab: Journal of South American Earth Sciences, v. 15, p. 39–57.
- Kozlowski, E.R., Manceda, R., and Ramos, V., 1993, Estructura, in Ramos, V., ed., Geología y Recursos Naturales de Mendoza: Relatorio del 12º Congreso Geológico Argentino y 2º Congreso de Exploración de Hidrocarburos, I (18), p. 235–256.
- Kretz, R., 1983, Symbols for rock-forming minerals: American Mineralogist, v. 68, p. 277–279.
- Kwak, T., and Tan, T., 1981, The importance of CaCl₂ in fluid composition trends—evidence from the King Island (Dolphin) skarn deposit: Economic Geology, v. 76, p. 955–960.
- La Rocque, J.A., 1964, Areas y Prioridades para la Prospección, Contrato N°1103, Informe N° 15: Dirección General de Fabricaciones Militares: Biblioteca del Servicio Geológico Minero Argentino, Buenos Aires, 106 p. and appendixes.
- Leake, B., Woolley, A., Arps, Ch., Birch, W., Gilbert, Ch., Grice, J., Hawthorne, F., Kato, A., Kisch, H., Krivovichev, V., Linthout, K., Laird, J., Mandarino, J., Marensch, W., Nickel, E., Rock, N., Schumacher, J., Smith, D., Stephenson, N., Ungaretti, L., Whittaker, E., and Youzhi, G., 1997, Nomenclature of amphiboles: Report of the subcommittee on amphiboles of the International Mineralogical Association, Commission on New Minerals and Mineral Names: American Mineralogist, v. 82, p. 1019–1037.
- Legarreta, L., Gulisano, C.A., and Uliana, M.A., 1993, Las secuencias Sedimentarias Jurásico-Cretácicas, in Ramos, V.A., ed., Geología y Recursos Naturales de Mendoza: Relatorio del XII Congreso Geológico Argentino y II Congreso de Exploración de Hidrocarburos, I (9), p. 87–114.
- López-Escobar, L., Cembrano, J., and Moreno, H., 1995, Geochemistry and tectonics of the Chilean Southern Andes basaltic Quaternary volcanism (37–46°S): Revista Geológica de Chile, v. 22, p. 219–234.
- Lurgo, C., and Zappettini, E., 1987, Informe Final del catedo Aguas Amarillas, Departamento Malargüe, provincia de Mendoza, Dirección General de Fabricaciones Militares, Buenos Aires: Biblioteca del Servicio Geológico Minero Argentino, Buenos Aires, 15 p. and appendixes.
- Maksaev, V., and Zentilli, M., 2002, Chilean strata-bound Cu- (Ag) deposits: An overview, in Porter, T., ed., Hydrothermal iron oxide copper-gold and related deposits: A global perspective: Adelaide, PGC Publishing, v. 2, p. 185–205.
- Marschik, R., and Fontboté, L., 2001, The Candelaria-Punta del Cobre iron Oxide Cu-Au (-Zn-Ag) Deposits, Chile: Economic Geology, v. 96, p. 1799–1827.
- McLeod, R.L., and Stanton, R.L., 1984, Phyllosilicates and associated minerals in some Paleozoic stratiform sulfide deposits of Southwestern Australia: Economic Geology, v. 79, p. 1–23.
- Meinert, L., 1995, Compositional variation of igneous rocks associated with skarn deposits—Chemical evidence for a genetic connection between petrogenesis and mineralization, in Thompson, J.F., ed., Magmas, fluids, and ore deposits: Mineralogical Association of Canada, Short Course Series, v. 23, p. 401–418.
- Meinert, L.D., Dipple, G.M., and Nicolescu, S., 2005, World skarn deposits, in Hedenquist, J.W., Thompson, J.F.H., Goldfarb, R.J., and Richards, J.P., eds., Economic Geology 100th Anniversary Volume: Society of Economic Geologists, Littleton, Colorado, USA, Includes supplementary appendices on CD-ROM (filename: Meinert), p. 299–336.
- Méndez, V., Zanettini, J.C., and Zappettini, E., 1995, Geología y Metalogénesis del Orógeno Andino Central, Dirección Nacional del Servicio Geológico: Secretaría de Minería de la Nación, Anales N° 23, 190 p.
- Middlemost, E., 1994, Naming materials in the magma/igneous rock system: Earth Science Reviews, v. 37, p. 215–224.
- Mingramm, A., González Segura, J., and Nocioni, A., 1993, Fold belt tectonic of the Malargüe area, Central West Argentina: XII Congreso Geológico Argentino y II Congreso de Exploración de Hidrocarburos, v. 3, p. 179–187.
- Moody, T.C., Hawkes, N., Ramos, D., Loader, S., Paney, R., Abbott, C., Carbonell, J., and Sillitoe, R.H., 2003, The Marcona iron oxide copper deposits, Perú: 3rd Congreso Internacional de Prospectores y Exploradores, Lima, Conferencias, Instituto de Ingenieros de Minas del Perú, Lima, Proceedings CD-ROM, 2 p.
- Morimoto, N., Fabries, J., Ferguson, A.K., Ginzburg, I.V., Ross, M., Seifert, F.A., Zussman, J., Aoki, K., and Gottardi, G., 1988, Nomenclature of pyroxenes: American Mineralogist, v. 73, p. 1123–1133.
- Morris, J.D., and Hart, S.R., 1983, Isotopic and incompatible element constraints on the genesis of island arc volcanics, Cold Bay and Amak Island, Aleutians: Geochimica et Cosmochimica Acta, v. 47, p. 2015–2030.
- Mpodozis, C., and Ramos, V., 1998, The Andes of Chile and Argentina, Cordillera de los Andes geological and mining potential: The new tectonic and metallogenic approach: International Symposium, Mendoza, Argentina, Proceedings, p. 59–90.
- Naciones Unidas, 1970, Investigación sobre mineral de cobre porfídico en las provincias de Mendoza, Neuquén y San Juan, Argentina: New York, Programa de las Naciones Unidas para el Desarrollo, U.N., 356 p.
- Newman, A., and Brown, G., 1987, The chemical constitution of Clays, in Newman, A., ed., Chemistry of clays and clay minerals: Mineralogical Society, Monograph

- nº 6, p. 1–129.
- Nullo, F., 1985, Descripción Geológica de la Hoja 29 a Cerro Campanario, Mendoza: Servicio Geológico Nacional: Buenos Aires, Biblioteca del Servicio Geológico Minero Argentino, 53 p.
- Nullo, F.E., Stephens, G.C., Otamendi, J., and Baldauf, p. E., 2002, El volcanismo del Terciario superior del sur de Mendoza: Revista de la Asociación Geológica Argentina, v. 57 (2), p. 119–132.
- Nyström, J., and Henríquez, F., 1994, Magmatic features of iron ores of the Kiruna type in Chile and Sweden: Ore textures and magnetite geochemistry: Economic Geology, v. 89, p. 820–839.
- Ohmoto, H., 2003, Nonredox transformations of magnetite-hematite in hydrothermal systems: Economic Geology, v. 98, p. 157–162.
- Pearce, J.A., 1996, A user's guide to basalt discrimination diagrams, in Wyman D.A., ed, Trace element geochemistry of volcanic rocks: Applications for massive sulphide exploration: Geological Association of Canada, Short Course Notes, v. 12, p. 79–114.
- Peña, A., 1955, Informe y Exploración Yacimientos de Hierro, Zona Sur, Mendoza, Dirección Nacional de Minería, Delegación Mendoza: Biblioteca del Servicio Geológico Minero Argentino, Buenos Aires, 59 p. and appendixes.
- Pollard, p., 2000, Evidence of a magmatic fluid and metal source for Fe-oxide Cu-Au mineralization, in Porter, T.M., ed, Hydrothermal iron oxide copper-gold and related deposits: A global perspective: Adelaide, Australian Mineral Foundation, p. 27–41.
- Pons, M.J., Franchini, M.B., and Meinert, L.D., 2004, Geochemical characterization of Neogene magmatism linked to skarn mineralization, SW Mendoza, Argentina: 32nd International Geological Congress, Florence, Italy, Abstracts with Programs, Poster Presentation, v. 32, part 2, p. 917.
- Ramos, V.A., 1993, Interpretación Tectónica, in Ramos, V.A. ed., Geología y Recursos Naturales de Mendoza: Relatorio del XII Congreso Geológico Argentino y II Congreso de Exploración de Hidrocarburos, I (19), p. 257–266.
- Ramos, V.A., 1999a, Las Provincias Geológicas del Territorio Argentino: Instituto de Geología y Recursos Minerales, Servicio Geológico Minero Argentino, SEGEMAR, Anales 35, 1, p. 41–96.
- Ramos, V.A., 1999b, Rasgos estructurales del territorio Argentino: Instituto de Geología y Recursos Minerales, Servicio Geológico Minero Argentino, SEGEMAR, Anales 29, (24), p. 715–784.
- Ramos, V.A., and Nullo, F., 1993, El Volcanismo de Arco Cenozoico, in Ramos, V.A., ed., Geología y Recursos Naturales de Mendoza: Relatorio del XII Congreso Geológico Argentino y II Congreso de Exploración de Hidrocarburos, I (19), p. 149–160.
- Rigal, R., 1942, Los yacimientos de magnetita de Hierro Indio y otros menores del Departamento San Rafael, provincia de Mendoza, Dirección de Minas y Geología: Biblioteca del Servicio Geológico Minero Argentino, Buenos Aires, Boletín nº 52: 27 p. and appendixes.
- Sangster, D.F., 1969, The contact metasomatic magnetite deposits of south-western British Columbia: Geological Survey of Canada, Bulletin 172, 85 p.
- Schwartz, M.O., and Melchor, F., 2004, The Falémé iron district, Senegal: Economic Geology, v. 99, p. 917–939.
- Shiga, Y., 1988, Silicic magnetite from the Kamaishi mine, Japan: Mining Geology, v. 38, p. 437–440.
- Sillitoe, R.H., 2003, Iron oxide copper-gold deposits: An Andean view: Mineralium Deposita, v. 38, p. 787–812.
- Tabachi, M.H., and Elizalde, C.O., 1961, Informe preliminar sobre las manifestaciones ferríferas del Cajón del Yeso, departamento Malargüe, Mendoza, Dirección General de Fabricaciones Militares: Biblioteca del Servicio Geológico Minero Argentino, Buenos Aires, 37 p. and appendixes.
- Tormey, D.R., Hickey Vargas, R., Frey, F., and López-Escobar, L., 1991, Recent lavas from the Andean volcanic front (33 to 42°S), interpretations of along-arc compositional variations: Geological Society of America, Special Paper 265, p. 57–78.
- Vivallo, W., and Henriquez, F., 1998, Génesis común de los yacimientos estratoligados y vetiformes de cobre del Jurásico Medio a Superior en la Cordillera de la Costa, Región de Antofagasta, Chile: Revista Geológica de Chile, v. 25, p. 199–228.
- Vivallo, W., 2005, Yacimientos de Oxidos de Hierro-Cobre-Oro en Chile: Actas del 16º Congreso Geológico Argentino, La Plata, Tomo 2, p. 397–402.
- Westendorp, R.W., Watkinson, D.H., and Jonasson, I.R., 1991, Silicon-bearing zoned magnetite crystals and the evolution of hydrothermal fluids at the Ansil Cu-Zn mine, Rouyn-Noranda, Quebec: Economic Geology, v. 86, p. 1110–1114.
- Williams, P.J., 1999, Fe oxide Cu-Au deposits of the Olympic Dam/Ernest Henry type, in Hodgson, C.J. and Franklin, J.M., eds., New developments in the geological understanding of some major ore types and environments, with implications for exploration: Prospectors and Developers Association of Canada, Short Course, Toronto, p. 1–43.
- Williams, p., Barton, M., Johnson, D., Fontboté, Ll., De Haller, A., Mark, G., and Oliver, N., 2005, Iron oxide copper-gold deposits: Geology, space-time distribution, and possible modes of origin: Economic Geology 100th Anniversary Volume, p. 371–405.
- Wippern, J., 1974, Informe final área de reserva nº 9 "Las Cuevas", Mendoza, Dirección General de Fabricaciones Militares: Biblioteca del Servicio Geológico Minero Argentino, 23 p. and appendixes.
- Xu, J.H., and Zhang, X.F., 1998, Mineralogic, isotopic, and fluid inclusion study of the Qinglongshan iron skarn deposit at the south margin of the Binjiang granite, south Anhui, China: Ninth Quadrennial IAGOD Symposium, Beijing, 1994: Stuttgart, Schweizerbart'sche Verlags-handlung, Proceedings, p. 427–439.
- Zanettini, J.C., 1984, Prospección Mendoza Sur, Informe final proyecto Santa Clara y Mendoza Sur, Dirección General de Fabricaciones Militares: Biblioteca del Servicio Geológico Minero Argentino, Buenos Aires, 46 p. and appendixes.

- Zanettini, J.C., 1999, El yacimiento ferrífero Hierro Indiano, Mendoza: Instituto de Geología y Recursos Minerales, Servicio Geológico Minero Argentino, Anales 35, p. 1547–1552.
- Zanettini, J.C., and Carotti, M.A., 1993, Yacimientos Metálicos y Metalogénesis, *in* Ramos, V.A., ed., Geología y Recursos Naturales de Mendoza: Relatorio del XII Congreso Geológico Argentino y II Congreso de Exploración de Hidrocarburos, Mendoza, Argentina, IV (1), p. 485–504.
- Zürcher, L., Ruiz, J., and Barton, M.D., 2001, Paragenesis, elemental distribution, and stable isotopes at the Peña Colorada iron skarn, Colima, Mexico: Economic Geology, v. 96, p. 535–557.

